

IRX-CIGALE: a tailored module for Low-Luminosity AGN

I. E. López^{1,2*}, G. Yang^{3,4}, G. Mountrichas⁵, M. Brusa^{1,2}, D. M. Alexander⁶, R. D. Baldi⁷, E. Bertola⁸, S. Bonoli^{9,10},
A. Comastri², F. Shankar¹¹, N. Acharya⁹, A. V. Alonso Tetilla¹¹, A. Lapi¹², B. Laloux^{6,13}, X. López López^{1,2},
I. Muñoz Rodríguez^{11,13}, B. Musiimenta^{1,2}, N. Osorio Clavijo¹⁴, L. Sala¹⁵, and D. Sengupta^{1,2}

¹ Dipartimento di Fisica e Astronomia "Augusto Righi", Università di Bologna, via Gobetti 93/2, 40129 Bologna, Italy

² INAF - Osservatorio di Astrofisica e Scienza dello Spazio di Bologna, via Gobetti 93/3, 40129 Bologna, Italy

³ Kapteyn Astronomical Institute, University of Groningen, P.O. Box 800, 9700 AV Groningen, The Netherlands

⁴ SRON Netherlands Institute for Space Research, Postbus 800, 9700 AV Groningen, The Netherlands

⁵ Instituto de Física de Cantabria (CSIC-Universidad de Cantabria), Avenida de los Castros, 39005 Santander, Spain

⁶ Centre for Extragalactic Astronomy, Department of Physics, Durham University, Durham, DH1 3LE, UK

⁷ INAF - Istituto di Radioastronomia, via Gobetti 101, 40129 Bologna, Italy

⁸ INAF - Osservatorio Astrofisico di Arcetri, Largo E. Fermi 5, 50125, Firenze, Italy

⁹ Donostia International Physics Center (DIPC), Manuel Lardizabal Ibilbidea, 4, Donostia-San Sebastián, Spain

¹⁰ IKERBASQUE, Basque Foundation for Science, E-48013, Bilbao, Spain

¹¹ School of Physics and Astronomy, University of Southampton, Highfield, Southampton SO17 1BJ, UK

¹² SISSA, Via Bonomea 265, 34136 Trieste, Italy

¹³ Institute for Astronomy & Astrophysics, National Observatory of Athens, V. Paulou & I. Metaxa 11532, Greece

¹⁴ Instituto de Radioastronomía y Astrofísica (IRyA-UNAM), 3-72 (Xangari), 8701, Morelia, Mexico

¹⁵ Universitäts-Sternwarte, Fakultät für Physik, Ludwig-Maximilians-Universität, Scheinerstr.1, 81679 München, Germany

April 29, 2024

ABSTRACT

The spectral energy distribution (SED) of low-luminosity active galactic nuclei (LLAGN) poses distinct challenges, primarily due to their radiation being comparable to their host galaxy and the complex accretion physics involved. This study unveils a novel module tailored for the CIGALE framework, explicitly aimed at the intricacies of SED fitting for LLAGN. This innovative module combines the empirical $L_X-L_{12\mu\text{m}}$ relationship with physically grounded accretion models, specifically advection-dominated accretion flows (ADAFs) and truncated accretion disks, to more precisely depict LLAGN's central engine emissions.

Applied to a curated selection of 52 X-ray-detected local galaxies, mainly LINERs and Seyferts, we conducted an extensive analysis to evaluate the module's accuracy against higher-luminosity AGN from the COSMOS and SDSS datasets. Our module proves adaptable at estimating bolometric luminosities with remarkable accuracy, even amid significant galaxy contamination. We also introduce an X-ray bolometric correction formula spanning ten orders of magnitude in luminosity.

We also analyzed the α_{ox} , the index representing the slope between the UV and X-ray emissions, revealing unique trends diverging from high-luminosity AGN. Contrary to quasars, where α_{ox} correlates with λ_{Edd} , LLAGN exhibit either a constant or weakly correlated α_{ox} values. This variance highlights a shift in accretion dynamics and photon production in the low luminosity regime. Furthermore, for these LLAGN, we observe a decrease of 1.4 dex in specific star formation rates from the entire galaxy to a central 9-arcsecond aperture, suggesting a possible indication of a feedback mechanism in these sources.

Our insights affirm the critical role of a multiwavelength strategy in AGN research, revealing a distinct behavior for LLAGN from that of quasars. This contribution significantly enriches our comprehension of LLAGN, providing a robust framework for future studies to provide a complete census of the AGN population.

Key words. galaxies: active — active galactic nuclei: low-luminosity — techniques: spectral fitting

1. Introduction

Active galactic nuclei (AGN) are extremely luminous objects fueled by accretion onto supermassive black holes at the cores of galaxies (Alexander & Hickox 2012). Their influence significantly shapes the evolution of host galaxies (e.g., Fabian 2012) and plays a crucial role in regulating star formation and feedback processes (e.g., Heckman & Best 2014). AGN exhibit diverse spectral and temporal variability, posing challenges for their classification and comprehension. A standard categorization method is based on luminosity, where typical AGN, like quasars (QSOs), have bolometric luminosities exceeding

10^{44} erg s⁻¹, while low-luminosity AGN (LLAGN) display lower luminosities (Peterson 1997).

LLAGN can be defined as galaxies with X-ray luminosities less than 10^{42} erg s⁻¹ and additional evidence of nuclear activity, such as AGN-like spectra (Ptak 2001). This category often includes Low-Ionization Nuclear Emission-line Regions (LINERs, Ho 1999). Seyferts, with generally higher luminosities, are typically categorized directly as AGN. However, exceptions exist, as seen in the case of low-luminosity Seyferts like NGC 1566 (Agüero et al. 2004). Behind these blurred boundaries, the community keeps debating whether LLAGN are downscaled versions of their brighter counterparts (e.g., Maoz 2007) or whether they are dominated by different accretion physics (e.g., Ishibashi et al. 2014).

* e-mail: ielopez.astro@gmail.com

In the local Universe, LLAGN are more common than QSOs. The steep luminosity function of AGN suggests that LLAGN could be more prevalent at all redshifts than previously assumed, as indicated by various studies (e.g., Schawinski et al. 2009; Aird et al. 2012). Despite their prevalence, their nature is not fully understood due to lower luminosity compared to brighter AGN (Padovani et al. 2017; Hickox & Alexander 2018). While AGN are known to significantly influence galaxy evolution through AGN feedback mechanisms, the potential role of LLAGN in galaxy evolution has not been fully elucidated.

LLAGN can hide compact jets and release kinetic energy through them (e.g., Fernández-Ontiveros et al. 2023). Unlike the massive jets observed in radio-loud AGN, the lower-power jets from LLAGN may remain confined within the host galaxy, substantially affecting the interstellar medium (ISM) and altering star formation processes (Mukherjee et al. 2018). LINERs can be radio-quiet or radio-loud, with low-accreting black holes that launch sub-relativistic and relativistic jets, respectively (Baldi et al. 2021a). Beyond kinetic feedback, winds from sustained radiatively inefficient accretion can also suppress star formation (Almeida et al. 2023). For instance, in the Sombrero galaxy, winds—driven either by radiatively inefficient accretion or by jets—induce outflows exceeding 1000 km/s (Goold et al. 2023). Similarly, in the massive spiral galaxy NGC 4579, a radio jet confined to the host galaxy generates low-velocity shocks and turbulence, significantly influencing the ISM by heating the inner kpc and suppressing star formation (Ogle et al. 2024). Although these examples provide insights into the impacts on individual sources, as a collective, LLAGN might play a pivotal role in galaxy evolution, a role that is yet to be fully characterized. The high accretion phase of an AGN lasts only 5-10% of its duty cycle, with most of its cycle being in a low-accreting phase (Novak et al. 2011). Furthermore, local LLAGN may be the relics of previously high-accreting AGN. A comprehensive understanding of LLAGN properties and their evolution is vital for a thorough perspective on AGN and galaxy evolution.

While the luminosity definition of LLAGN allows for the possibility of high-accreting low-mass black holes, the local population of LLAGN generally exhibits low accretion rates ($\log \lambda_{\text{Edd}} < -3$, Ho 2009). The accretion process in LLAGN is to occur through a radiatively inefficient mode, where gas cannot efficiently radiate its thermal energy due to either low density or strong magnetic fields. This leads to lower radiative efficiency and a harder X-ray spectrum (product of the optically thin free-free emission), distinguishing them from higher-luminosity AGN. Additionally, LLAGN lack a big-blue bump associated with the blackbody radiation of the internal orbits of a thin accretion disk; instead, they show a red-bump (Ho 2008).

At low accretion rates, the accretion flow becomes less dense, optically thin, and less effective at cooling. Consequently, the standard accretion disk (geometrically thin, optically thick disks) becomes unstable and is supplanted by another mechanism. The exact mechanism driving accretion in LLAGN is still debated, with proposed models including hot, advection-dominated accretion flows (ADAF), adiabatic inflow-outflow solutions (ADIOS), and convection-dominated accretion flows (CDAF; for a review, see Yuan & Narayan 2014). Additionally, standard accretion disks truncated at an inner radius and hybrid models combining truncated disks with hot flows are considered plausible mechanisms (Taam et al. 2012; Bu & Yang 2019). Clarifying the nature of the accretion flow in LLAGN is essential for understanding their evolution, fueling mechanisms, and the growth of supermassive black holes in the local universe.

The identification and characterization of LLAGN present challenges due to their lower brightness and potential contamination from star formation and X-ray binaries (e.g., Annuar et al. 2020). Spectral energy distribution (SED) fitting, utilizing multi-wavelength data, emerges as a powerful tool for addressing these challenges. SED fitting can be used to disentangle different physical mechanisms at play from the AGN and its host galaxy, providing insights into accretion disk and dusty torus properties, as well as host galaxy characteristics such as star formation rate (SFR) and stellar mass (M_*). Crucially, SED fitting is the optimal method for obtaining the AGN bolometric luminosities.

Various SED-fitting popular codes are available and have recently been shown to yield similar distributions of general physical parameters (Pacifi et al. 2023). One of them is Code Investigating GALaxy Emission (CIGALE¹; Boquien et al. 2019). CIGALE leverages the wealth of information in multi-wavelength data by incorporating related processes as priors in Bayesian fits. Including the X-ray component in the AGN model, commonly referred to as X-CIGALE and included inside the last CIGALE release, has expanded the capabilities of CIGALE (Yang et al. 2020, 2022). X-CIGALE incorporates a power law to model the intrinsic hot corona emission based on the slope between the X-ray emission at 2 keV and UV at 2500 Å (α_{ox} , Just et al. 2007). This relationship is expected due to the accretion disk emission peaking in the UV, with the X-ray emission produced in the corona believed to be Compton up-scattering of the UV photons (Haardt & Maraschi 1993). With this and other improvements, X-CIGALE has been applied to study various aspects of AGN, including star formation history, AGN feedback, and black hole accretion on local mass scaling relations (e.g., Masoura et al. 2021; Mountrichas et al. 2022; López et al. 2023). However, in contrast to the $L_{2500\text{Å}}-\alpha_{\text{ox}}$ relation well-established for high-luminosity QSOs (e.g., Lusso et al. 2010), the relation for LLAGN remains elusive, perhaps due to intrinsic differences in the accretion process.

A promising avenue for investigating LLAGN is the $L_X-L_{12\mu\text{m}}$ relation, establishing a connection between intrinsic X-ray luminosity (2-10 keV) and the nuclear 12 micron luminosity, as shown by Gandhi et al. (2009). These emissions share a common bond since mid-infrared (MIR) emission is also reprocessed UV emission. The nuclear dust absorbs the emission generated by accretion and reemits it thermally in the IR. This relation has been systematically explored across various luminosity regimes and seems valid for Seyferts and LINERs in the luminosity regime $L_X = 10^{40}-10^{45}$ erg s⁻¹ (Asmus et al. 2015; Fernández-Ontiveros et al. 2023). Additionally, it has already been incorporated into SED fitting methodologies, providing an alternative approach to link X-ray emission with optical-IR emission (Duras et al. 2020).

This study introduces a novel X-ray module into the widely utilized SED fitting code CIGALE. This module integrates two principal components: the $L_X-L_{12\mu\text{m}}$ relationship, employed as a prior, and a central accretion engine modeled as an ADAF, complemented by an optional truncated accretion disk. Section 2 offers an in-depth examination of the code and this innovative module. Section 3 demonstrates the application of this module on a X-ray-detected sample of 52 local LLAGN. We elucidate our methodological approach for acquiring X-ray intrinsic fluxes, UV-to-FIR photometry, and SED fitting parameters. Moreover, we present secondary AGN samples to validate the $L_X-L_{12\mu\text{m}}$ relation. Section 4 details the outcomes, starting with validating our methodology for the secondary AGN samples and

¹ <https://cigale.lam.fr>

comparing our findings for the LLAGN with those from previous studies. We analyze the X-ray bolometric correction, extending down to the lower limit of $L_{\text{Bol}} = 10^{39} \text{ erg s}^{-1}$. Furthermore, we address the issue of galaxy contamination, investigate α_{ox} parameter for LLAGN, noting deviations from QSO extrapolations, and assess the influence of LLAGN on star formation, comparing it with a sample of high-luminosity AGN. Section 5 synthesizes our findings and conclusions, highlighting how this new CIGALE module furnishes a potent toolkit for probing the lower-luminosity regime. This advancement will facilitate the study of supermassive black holes in states of low accretion and is poised to augment future AGN censuses, thereby enriching our comprehension of the role these LLAGN play in the evolution of galaxies.

2. The Code

2.1. Motivation

CIGALE is recognized as a powerful multiwavelength SED template fitting tool tailored for extragalactic research (Boquien et al. 2019). It can accurately derive physical parameters spanning the X-ray to radio spectrum, meticulously accounting for dust attenuation in the UV-optical and its corresponding infrared re-emission via energy balance. This process involves fitting observed SEDs with a user-generated model library incorporating diverse physical templates. The likelihood distribution is computed using each fit, and a Bayesian-like analysis allows for extracting key physical parameters.

Notable enhancements to CIGALE were done by Yang et al. (2020, 2022), particularly the integration of an X-ray module and the SKIRTOR AGN model (Stalevski et al. 2012, 2016). The X-ray module employs the $\alpha_{\text{ox}}-L_{2500\text{\AA}}$ relation from Just et al. (2007) as a foundational prior, bridging UV photons from the accretion disk with X-rays from the corona. This well-established relation for QSOs correlates the intrinsic AGN luminosity at 2500Å with α_{ox} , the SED slope between 2500Å UV and two keV X-ray bands, as modeled in a standard scenario where UV-optical photons are inverse-Compton scattered to X-ray energies (Haardt & Maraschi 1991).

The SKIRTOR model encapsulates emissions from three AGN main components: the accretion disk, polar dust, and a clumpy torus. Notably, for the emission of the accretion disk—also referred to as the central engine or seed photons—CIGALE adopts a range of parametric disk models. This allows introducing a delta parameter (δ_{AGN}) to modulate the power-law slope within the 0.125 to 10-micron range. Specifically, for the accretion disk from Schartmann et al. (2005):

$$\lambda L_{\lambda} \propto \begin{cases} \lambda^2 & 0.008 \leq \lambda \leq 0.05 [\mu\text{m}] \\ \lambda^{0.8} & 0.05 < \lambda \leq 0.125 [\mu\text{m}] \\ \lambda^{-0.5+\delta_{\text{AGN}}} & 0.125 < \lambda \leq 10 [\mu\text{m}] \\ \lambda^{-3} & 10 < \lambda \leq 1000 [\mu\text{m}] \end{cases} .$$

CIGALE also includes an alternative accretion disk model based on the original SKIRTOR disk, improved to better reproduce with observational data (Feltre et al. 2012), maintaining a similar form to the model described above.

Despite its efficacy across a broad wavelength range and its substantial contributions to galaxy astrophysics, CIGALE's application to LLAGN reveals notable limitations. For instance, while Maoz (2007) observed similarities between LLAGN and QSOs, suggesting potential model applicability, divergences in accretion flow-dominated UV photon populations in LLAGN

challenge the universal application of the $\alpha_{\text{ox}}-L_{2500\text{\AA}}$ relation. The complex accretion physics of LLAGN continues to fuel debate, highlighting the need for tailored approaches rather than relying on universally applied relations.

Ho (2008) show fundamental discrepancies in LLAGN SEDs relative to QSOs, notably below $\log \lambda_{\text{Edd}} < -3$, characterized by a dominant red bump over the expected big blue bump. This discrepancy complicates the direct application of QSO models to LLAGN. Additional studies, such as Xu (2011), have explored the $\alpha_{\text{ox}}-L_{2500\text{\AA}}$ relation for samples of Seyferts and LINERs, revealing certain similarities with established QSO calibrations. However, their determination of $L_{2500\text{\AA}}$ is through proxies derived from H β and B-band ($\sim 4420 \text{\AA}$) extrapolation. Even in models assuming LLAGN as scaled versions of QSOs, pure ADAF models deviate slightly from the $L_{2500\text{\AA}}-\alpha_{\text{ox}}$ relation observed in QSOs (Maoz 2007). Furthermore, Esparza-Arredondo et al. (2020) demonstrated that certain faint AGN deviate from the expected relation. Nemmen et al. (2014), through a physically motivated SED fitting, predicted an α_{ox} for LLAGN far from extrapolations of its high-luminosity counterparts, emphasizing the influence of radiatively inefficient accretion processes.

To overcome the challenges posed by the unique accretion physics of LLAGN, we propose a novel X-ray module (IRX) designed specifically for these sources. Recognizing the current uncertainties in their accretion physics and the need for a more customized approach, we propose two main changes: the seed photons from the central engine and the prior link of the X-ray emission to the rest of the SED.

Nonetheless, the current adaptation of this module introduces a critical caveat. Given that an ADAF has a considerable synchrotron emission it can also be observed in the radio and submillimeter (sub-mm) wavelengths, so careful consideration is required for another important component of the AGN framework: radio jets. Typically, radio jets are accounted for exclusively within radio frequencies for high-luminosity AGN. The radio module extends to the far-IR in CIGALE, modeling the synchrotron emission as a power law. This specificity enables the distinct determination of the spectrum slope, differentiating it from other sources, such as star-forming regions, modeled with another power law with a different slope.

However, the emission from radio jets spans the entire electromagnetic spectrum, not just the radio domain. This omnipresence can complicate SED fittings that omit their modeling, leading to potential contamination of SEDs intended to map the photon production by SMBH accretion processes. As highlighted by Nemmen et al. (2014), while the typical ADAF exhibits a SED characterized by distinct bumps, the average jet emission in LLAGN manifests as a softer, more constant output across the spectrum from 100 microns to X-ray wavelengths. This spectral behavior makes it impossible to fit without a constraint from the radio bands. Because of that, in this work, jet emission will be neglected in the X-ray to IR analysis. In future studies, we will incorporate the ADAF emission into the radio module of CIGALE, facilitating the differentiation between potential jet models and ADAFs. This development will allow for precisely fitting and identifying sub-mm and radio emissions in LLAGN, thereby excluding potential synchrotron interference in the broader spectrum. Such advancements will enable us to avoid possible synchrotron emission in the rest of the spectra and thus model the total emission from an AGN more accurately and better understand the role of jets in LLAGN activity.

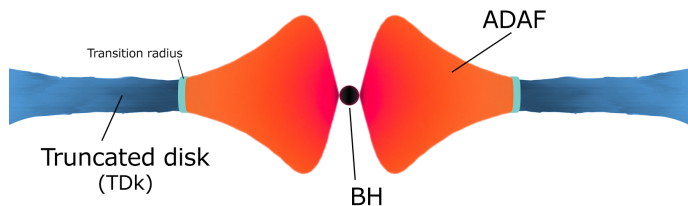


Fig. 1. Schematic diagram of an advection-dominated accretion flow (ADAF), the truncated accretion disk (TDk), and the transition radius.

2.2. The new module

We have introduced two main modifications to enhance the utility of CIGALE’s AGN model for LLAGN.

Firstly, the modeling of seed photons emanating from the central engine has been refined by incorporating a combination of a truncated thin disk and an ADAF. A schematic view of the central engine is shown in Fig. 1. Traditional accretion disks, characterized as geometrically thin and optically thick, generate a SED that is the sum of blackbody emission². In contrast, ADAFs are hot, optically thin solutions, and quasi-spherical, with a SED produced by synchrotron radiation, Bremsstrahlung radiation, and inverse Compton scattering. A truncated disk emulates the blackbody spectrum like a standard disk, albeit without the innermost and hotter orbits responsible for UV photon production. The details of the implementation are described in Section 2.2.1.

Secondly, we revisit the connection between the X-ray module and the UV-to-IR SKIRTOR model. The traditional $\alpha_{\text{ox}} - L_{2500\text{\AA}}$ relation is replaced with an empirical $L_X - L_{12\mu\text{m}}$ relation (Asmus et al. 2015). This relation connects the intrinsic X-ray luminosity (2-10 keV) and the nuclear 12 micron luminosity. The details of this implementation are outlined in Section 2.2.2.

2.2.1. A new central engine

For the ADAF component, we parameterize the mean SED based on the ADAF template from Nemmen et al. (2014). This module employs a physically motivated code, considering a hot, geometrically thick, optically thin two-temperature accretion flow with primary radiative processes being synchrotron emission, bremsstrahlung, and inverse Compton scattering. Our parameterization is limited to the UV-to-IR bands, as different CIGALE modules address radio and X-ray. The parameterization is as follows:

$$\lambda L_{\lambda}^{\text{ADAF}} \propto \begin{cases} \lambda^{1.5} & 0.008 \leq \lambda \leq 0.075 [\mu\text{m}] \\ \lambda^{1.15} & 0.075 < \lambda \leq 0.300 [\mu\text{m}] \\ \lambda^{1.45} & 0.300 < \lambda \leq 1.1 [\mu\text{m}] \\ \lambda^{0.95} & 1.1 < \lambda \leq 2.7 [\mu\text{m}] \\ \lambda^{0.45} & 2.7 < \lambda \leq 20 [\mu\text{m}] \\ \lambda^{-0.5} & 20 < \lambda \leq 100 [\mu\text{m}] \\ \lambda^{-3} & 100 < \lambda \leq 1000 [\mu\text{m}] \end{cases} . \quad (1)$$

In Nemmen et al. (2014), the option of a truncated accretion disk just outside the ADAF is also considered. These truncated disks are crucial for modeling an IR-bump not present in the non-thermal continuum (for an example, see Sombrero galaxy

² The disk can be modeled as a sum of rings, each emitting as a blackbody where its temperature depends on its distance from the SMBH.

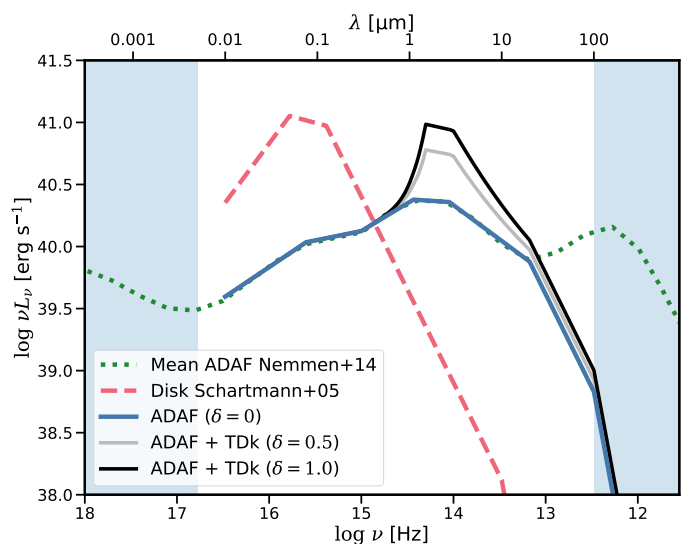


Fig. 2. SED for different accretion modes. The dotted green line represents the mean ADAF from Nemmen et al. (2014). The solid blue line illustrates the pure ADAF as parametrized in our work. At the same time, black and grey indicate the effects of altering the δ_{AGN} parameter, which introduces a truncated accretion disk. For comparative purposes, the dashed red line depicts the parametrization by Schartmann et al. (2005), commonly used in CIGALE for QSOs with standard accretion disks. The blue-shaded regions denote the wavelength ranges where the other modules of CIGALE operate, specifically X-ray on the left and Radio on the right.

in Fernández-Ontiveros et al. 2023). However, these two components are not independent, as they share bonding conditions with the ADAF. Furthermore, an external disk will reprocess the X-ray radiation produced by the ADAF. Fortunately, Nemmen et al. (2014) demonstrates that this effect is negligible, resulting in a SED identical to the standard disk. Building upon this, we separate both SED components and model the disk as follows:

$$\lambda L_{\lambda}^{\text{TDk}} \propto \begin{cases} \lambda^6 & 0.08 \leq \lambda \leq 1.5 [\mu\text{m}] \\ \lambda^{0.8} & 1.5 < \lambda \leq 3 [\mu\text{m}] \\ \lambda^{-0.5} & 3 < \lambda \leq 10 [\mu\text{m}] \\ \lambda^{-3} & 10 < \lambda \leq 1000 [\mu\text{m}] \end{cases} . \quad (2)$$

We have modified the δ_{AGN} parameter within CIGALE to introduce a scaling factor between a truncated disk and the ADAF continuum. With $\delta_{\text{AGN}} = 0$, the central engine is represented solely as an ADAF. Conversely, increasing values of δ_{AGN} indicate progressively stronger emissions from the truncated accretion disk relative to the ADAF. Figure 2 showcases the SED comparison between the standard QSO accretion disk model from Schartmann et al. (2005), the mean ADAF SED delineated by Nemmen et al. (2014), and our new UV-to-IR parametrization implemented in CIGALE. This comparison highlights the impact of varying δ_{AGN} on the relative strength of the truncated accretion disk within the total SED, illustrating the adjustable nature of our model in accommodating different LLAGN configurations. The total SED is given by:

$$\lambda L_{\lambda}^{\text{Total}} \propto \lambda L_{\lambda}^{\text{ADAF}} + \delta_{\text{AGN}} \times \lambda L_{\lambda}^{\text{TDk}} \quad (3)$$

This simplification allows the SEDs of both components to be managed independently, accommodating scenarios with and without a red bump.

2.2.2. A new way to connect X-ray to the SKIRTOR model

The decision to move away from the $\alpha_{\text{ox}}-L_{2500\text{\AA}}$ relation is motivated by the lack of reliable calibrations for this relation in the low-luminosity regime. Given that this relation links photons from the accretion disk with reprocessed emissions in the X-ray spectrum, changes in the UV photon population could significantly alter its calibration.

In contrast, the $L_X-L_{12\mu\text{m}}$ relation is based on a direct linkage between two different reprocessed photon types: X-ray and MIR. This relation has proven valid for a wide variety of AGN types, including Seyferts I, II, and LINERs, across five orders of magnitude up to $L_X \sim 10^{45} \text{ erg s}^{-1}$. Notably, this relation has been successfully utilized by [Duras et al. \(2020\)](#) for SED fitting, providing estimates of bolometric luminosity and corrections across various bands widely accepted in the field.

The $L_X-L_{12\mu\text{m}}$ relation is founded on the principle that UV-optical photons, originating from accretion physics, are reprocessed into X-rays by the corona and into IR by nuclear and polar dust. Interestingly, this relation appears unaffected by obscuration, exhibiting less than 0.1 dex differences between unobscured and highly obscured objects ([Asmus et al. 2015](#)). This stability is attributed to emissions from the polar outflow regions in the MIR and potentially higher covering factors in more obscured objects, which mitigate differences due to anisotropic viewing angles. This characteristic makes the relation particularly suitable for LLAGN, which, at low Eddington ratios, are believed to have high covering factors ($\sim 80\text{--}85\%$ [Ramos Almeida & Ricci 2017](#)). [Mason et al. \(2012\)](#) demonstrated the applicability of this relation to LLAGN using Spitzer data. Further validation is provided by [Fernández-Ontiveros et al. \(2023\)](#), who found that at sub-parsec resolution, all their LLAGN samples conformed to the $L_X-L_{12\mu\text{m}}$ relation as delineated by [Asmus et al. \(2015\)](#), confirming its broad applicability to LLAGN.

We implement this relation into the new X-ray module for CIGALE through the parameter α_{IRX} , defined as:

$$\alpha_{\text{IRX}} = \log \frac{L_{2-10 \text{ keV}}^{\text{int}}}{L_{12 \mu\text{m}}^{\text{nuc}}} \quad (4)$$

We have set α_{IRX} with a default value of 0.3, allowing for a minimum value of 0.0 and a maximum of 0.6, with intermediate values possible. This choice is supported by the findings of [Asmus et al. \(2015\)](#), where the dispersion is measured at 0.33. The calculation of $L_{12\mu\text{m}}^{\text{nuc}}$ in CIGALE considers the sum of the three AGN components (accretion disk, polar dust, and toroid), while $L_{2-10 \text{ keV}}^{\text{int}}$ is derived from the power-law fit for the AGN component due to the intrinsic nature of X-ray data. We assume the relationship holds at low luminosities because even at low accretion rates, both processes will be similarly affected due to the scarcity of UV photons. As usual, potential host contamination from X-ray binaries and host galaxy dust emissions will be accounted for in the grid models for SED fitting.

These refinements aim to provide a more precise and customized modeling strategy for LLAGN within the CIGALE framework. The code is accessible through the official CIGALE repository³. Although initially devised for CIGALE, the underlying concept is versatile and can be adapted for other computational frameworks. By addressing the existing model's limitations and uncertainties, we expect to enhance parameter ac-

curacy and achieve a more authentic depiction of the physical phenomena occurring in LLAGN.

3. Data and Fitting

This section describes the two samples used to evaluate the new CIGALE module presented in this work. The primary sample discussed in Section 3.1 comprises 52 local galaxies classified as Seyferts and LINERs. This sample will assess the LLAGN properties and validate the module's performance in the low luminosity regime. A subset of the primary sample, with independent bolometric luminosities, will be used to test the module's specific validity in this regime. As a secondary sample (Section 3.2), we use the COSMOS and SDSS QSO samples employed in previous CIGALE studies. These sources will be used to confirm the validity of our analysis's higher luminosity regime of the $L_X-L_{12\mu\text{m}}$ relation, a key underlying assumption. Finally, Section 3.3 discusses the fitting methodology and goodness of the fit.

3.1. LLAGN Sample

We compiled a sample of 52 local galaxies, each featuring a central X-ray detection with luminosities falling below $10^{44} \text{ erg s}^{-1}$. Characterized by low accretion rates, as indicated by their Eddington ratios ($\log \lambda_{\text{Edd}} < -3$), these galaxies are predominantly classified as radiatively inefficient accretion flow (RIAF) candidates. This classification suggests that the central engine might operate under a radiatively inefficient accretion mode ([Ho 2009](#)). The calculation of Eddington ratios was primarily based on bolometric corrections from X-ray luminosities, adopting a $k_X = 15.8$ as per [Ho \(2009\)](#), or through SED fitting for each source, as detailed in studies by [Eracleous et al. \(2010\)](#) and [Nemmen et al. \(2014\)](#).

Most of these galaxies are located within 40 Mpc and exhibit a size of less than five arcmin in radius. They span a wide range of morphologies, with their Hubble types ranging from -5 to 5. The SMBH masses, as retrieved from the literature, predominantly fall within the range of $7 < \log M_{\text{BH}} < 9$, though the sample includes several galaxies hosting less massive SMBHs. A comprehensive list of the galaxies and their characteristics can be found in Table 1, with the distributions of these properties depicted in Fig. 3.

In particular, ten galaxies were classified as Seyfert galaxies with low Eddington ratios: NGC2273, NGC3185, NGC3516, NGC3982, NGC4051, NGC4151, NGC4258, NGC4565, NGC4725, NGC5273. While the accretion regime is already inefficient, a standard accretion disk is not probable; sixty percent of them have independent evidence of showing radiatively inefficient accretion. Some galaxies show hints of having an ADAFs scenarios like NGC3516 ([Cao & Wang 2014](#)), NGC4258 ([Doi et al. 2005](#); [Szanecki et al. 2023](#)), NGC4565 ([Doi et al. 2005](#); [Liu & Wu 2013](#)) or NGC 5273 ([Giroletti & Panessa 2009](#)). NGC4051 are discussed to be a pure accretion flow scenario ([Peterson et al. 2000](#); [Meyer-Hofmeister & Meyer 2011](#)), or a truncated accretion disk with a comptonized region ([Zhang & Wu 2006](#)). NGC4151 is discussed to be a pure accretion flow scenario ([Niedźwiecki et al. 2015](#)), a truncated accretion disk ([Szanecki et al. 2021](#)) or a hybrid-scenario ([Alexander et al. 1999](#); [Mahmoud & Done 2020](#)).

The rest of the samples are classified as LINERs, from which all show evidence of hosting an AGN, mainly through the ionization power of its central X-ray emission (e.g., NGC2655,

³ The current version of this code is available on this branch: https://gitlab.lam.fr/cigale/cigale/-/tree/alpha_irx?ref_type=heads

ID	RA	Dec	z	Dist [Mpc]	log L_X [erg/s]	Ref
NGC1052	40.269	-8.2558	0.00496	19.19	41.20	2
NGC2273	102.536	60.8457	0.00613	29.76	40.89	1
NGC2685	133.894	58.7343	0.00295	13.26	39.00	2
NGC2655	133.909	78.2234	0.00467	23.82	41.20	2
NGC2768	137.906	60.0373	0.00451	22.07	39.73	1
NGC2787	139.826	69.2033	0.00232	7.41	39.20	1
NGC2841	140.511	50.9766	0.00211	14.51	38.94	1
NGC3031	148.888	69.0652	-0.00013	3.59	39.15	1
NGC3079	150.491	55.6799	0.00368	19.01	40.05	1
NGC3147	154.223	73.4007	0.00934	42.72	41.92	1
NGC3185	154.410	21.6883	0.00410	24.98	39.40	2
NGC3190	154.526	21.8326	0.00437	23.98	40.07	1
NGC3193	154.603	21.8940	0.00460	33.01	38.76	1
NGC3414	162.817	27.9750	0.00490	25.92	40.48	1
NGC3516	166.697	72.5685	0.00883	38.01	42.49	1
NGC3718	173.145	55.0679	0.00331	16.98	41.22	1
NGC3898	177.313	56.0843	0.00385	21.97	38.93	1
NGC3945	178.306	60.6755	0.00427	21.57	39.80	1
NGC3953	178.454	52.3266	0.00350	18.93	38.04	1
NGC3982	179.117	55.1252	0.00371	21.55	40.78	5
NGC4013	179.630	43.9468	0.00277	19.71	38.80	1
...

Table 1. Key properties of galaxies in the LLAGN sample. Distances are given in Mpc and X-ray luminosities in erg s^{-1} . The table includes references for the X-ray luminosities: 1 for Williams et al. (2022), 2 for González-Martín et al. (2009), 3 for Osorio-Clavijo et al. (2023), 4 for Yun et al. (2022), 5 for Kammoun et al. (2020), 6 for Cappi et al. (2006), and 7 for Masini et al. (2022).

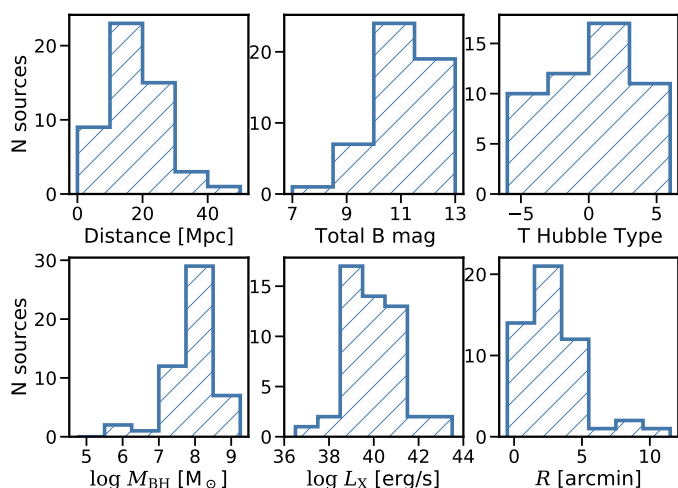


Fig. 3. Distributions illustrating the fundamental properties of the host galaxies and their associated supermassive black holes in the LLAGN sample considered in this work.

Reynaldi et al. 2020) or through radio nuclear emission with compact jets (e.g., Baldi et al. 2018, 2021b). For sixty percent of them, there are independent hints of an ADAF scenario or non standard accretion disk scenario: NGC1052 (Yuan et al. 2009; Falocco et al. 2020), NGC2787 (Doi et al. 2005; Pellegrini 2005; Liu & Wu 2013), NGC2841 (Pellegrini 2005), NGC3031 (Doi et al. 2005; Nemmen et al. 2014), NGC3079 (Chang et al. 2002), NGC3147 (Doi et al. 2005; Liu & Wu 2013), NGC3414 (Wójtowicz et al. 2023), NGC3718 (Doi et al. 2005), NGC4111 (Hauschild Roier et al. 2022), NGC4125 (Pellegrini 2005), NGC4138 (Liu & Wu 2013), NGC4203 (Doi et al. 2005; Yuan et al. 2009; Liu & Wu 2013), NGC4261 (Yuan et al. 2009; Nemmen et al. 2014; Pellegrini 2005), NGC4374 (Doi et al. 2005; Pellegrini 2005), NGC4438 (Pellegrini 2005), NGC4457 (Nemmen et al. 2014), NGC4486 (Doi et al. 2005; Nemmen

et al. 2014; Pellegrini 2005), NGC4494 (Nemmen et al. 2014), NGC4552 (Doi et al. 2005; Nemmen et al. 2014; Pellegrini 2005), NGC4579 (Doi et al. 2005; Nemmen et al. 2014; Yuan et al. 2009), NGC4594 (Nemmen et al. 2014; Pellegrini 2005; Liu & Wu 2013), NGC4698 (Tran et al. 2011), and NGC4736 (Nemmen et al. 2014; Liu & Wu 2013).

The primary X-ray catalogs utilized for sample compilation include Williams et al. (2022), Osorio-Clavijo et al. (2023), and González-Martín et al. (2009). These catalogs offer spectral fits to data from the Chandra and XMM-Newton telescopes, focusing on various models tailored to spectral features. Our emphasis is on the intrinsic emission from the corona or ADAF, characterized by power-law spectra. The extracted gamma (Γ) and normalization values for the power-law component were used to compute X-ray fluxes in both the soft (0.5-2 keV) and hard (2-10 keV) X-ray bands.

For specific sources, we utilized data from catalogs that incorporate reflection components, complex thermal elements, or torus models to understand their obscuration better. We used better constraints on the intrinsic power-law spectra of telescopes such as Swift-BAT or NuSTAR less affected by obscuration. For detailed information on individual sources, we refer to Yun et al. (2022) for NGC 5033, Kammoun et al. (2020) for NGC 3982, and Masini et al. (2022) for NGC 4258. Additionally, for NGC 4051, NGC 4151, and NGC 4725, the spectral fittings are taken from Cappi et al. (2006).

For each galaxy, we conducted photometry spanning UV to FIR bands using calibrated images from the DustPedia database⁴. We performed forced photometry in a 9-arcsecond radius aperture centered on each galaxy (refer to Fig. 4 for an example). This aperture covered GALEX NUV and FUV filters, ugriz SDSS bands, JHKs bands from 2MASS, Spitzer IRAC1-4 and WISE 1-4, Spitzer MIPS 24-70 microns, 100, Herschel PACS 70-100-160 microns, and Herschel SPIRE 250 microns. The 9-arcsecond radius was deliberately chosen to align with the diameter required to encompass the Full Width at Half Maximum (FWHM) of the Point Spread Function (PSF) for each filter in our analysis. Upper limits at 3σ were set for non-detected sources.

Using the Photutils library version 1.9⁵, we utilized a two-dimensional modeling approach to perform background calculations. To determine the background, we also implemented a sigma clipping technique and, where feasible, masked the galaxy using a mask derived from the largest isophote in the DustPedia database. Additionally, we applied aperture corrections and corrected for Milky Way extinction.

3.2. AGN Samples

We conducted validation tests using well-established datasets from high-luminosity AGN studies to verify the robustness of the hypothesis outlined in Section 2.2.2 regarding our newly developed IRX-CIGALE module. Specifically, we utilized the COSMOS and SDSS QSO samples referenced in previous CIGALE publications (Yang et al. 2020, 2022), enabling direct comparisons with established X-ray modules. These studies determined the bolometric luminosity of AGN using the α_{ox} prior, which we adopted as a benchmark to assess the robustness of our new prior.

The SDSS sample consists of type 1 AGN that are optically selected from the DR14 quasar catalog (Pâris et al. 2018), in-

⁴ <http://dustpedia.astro.noa.gr/Data>

⁵ <https://photutils.readthedocs.io/>

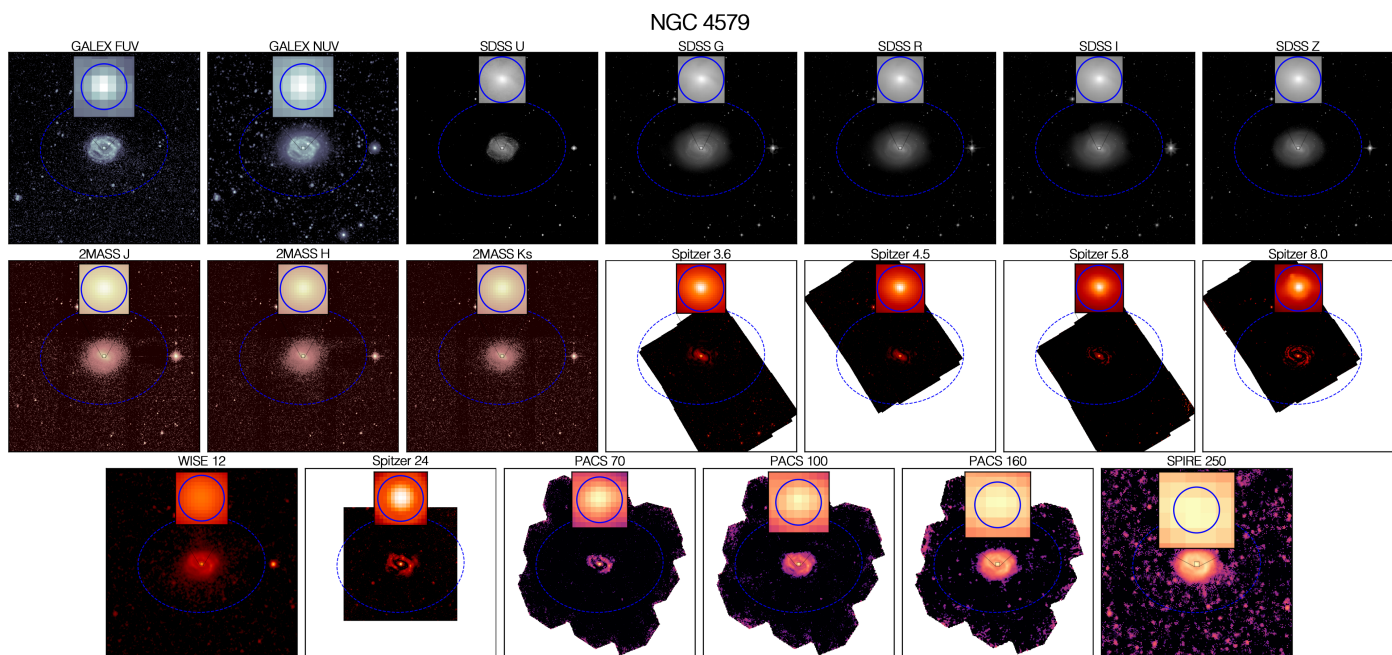


Fig. 4. Example of forced aperture photometry with a 9-arcsecond radius, executed across all wavelengths from GALEX NUV to Herschel SPIRE 250 microns. The blue ellipse delineates the galaxy’s boundary as identified by isophotes from DustPedia. An inset offers a detailed view of the 9-arcsecond aperture region utilized in this analysis, showcased as a blue circle.

cluding 1986 AGN detected in the 2–12 keV X-ray band with XMM-Newton at a significance level greater than 3σ . Galactic extinction corrections were applied to ensure the reliability of this dataset. The COSMOS sample, derived from the COSMOS-Legacy survey, comprises 590 X-ray-selected AGN with photometric data sourced from the COSMOS2015 catalog (Laigle et al. 2016) that spans 14 broad optical and infrared bands. Redshift measurements were taken from Marchesi et al. (2016).

For both the SDSS and COSMOS samples, the SED fitting methodology followed the parameters established in Yang et al. (2020), keeping the classic accretion disk model from Schartmann et al. (2005) and incorporating the new module using the α_{ir} for comparative analysis (see Section 4.1).

3.3. LLAGN Fitting

The SED fitting process for the LLAGN sample was conducted using a combination of CIGALE modules, comprehensively modeling both AGN and host galaxy emissions. The host galaxy characterization was performed using a Chabrier (2003) initial stellar mass function (IMF) with two possible metallicity values, a delayed star formation history for the stellar population and accounting for dust extinction. Dust emissions were effectively modeled using the Themis module (Jones et al. 2017). For the AGN component, seed photons were modeled using our novel ADAF + TDK approach, detailed in Section 2.2. This method allows adjustable parameters to explore the relevance of the truncated disk with δ_{AGN} values set at 0 and 1.0, accommodating a wide range of AGN fractions. The toroid’s opening angle was set at 70° , achieving a covering factor of 80% to model better the type of obscuration typical in low-accreting sources (Ricci et al. 2017). Viewing angles were adjusted to allow a direct view of the central engine ($i = 10^\circ$) or complete cover ($i = 80^\circ$), with intermediate angles tested but showing no significant impact on the results. The X-ray module was also employed to model emissions from the host galaxy, accounting for emissions from X-ray

binaries and the AGN X-ray power law across a range of power indexes. A detailed list of the parameters used in the CIGALE input is presented in Table 2.

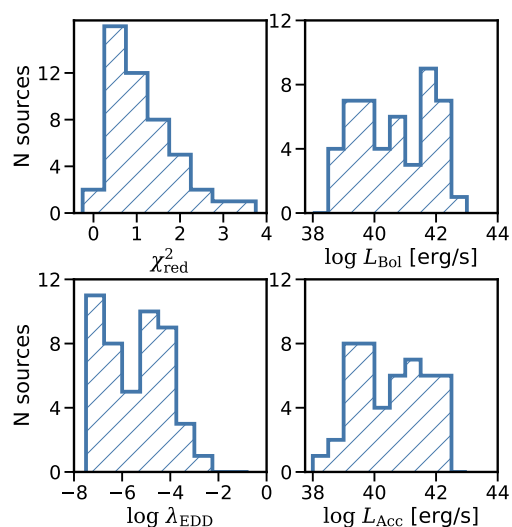


Fig. 5. Distribution of reduced chi-square (χ^2_{red}) values and key AGN properties derived from the SED fitting of the LLAGN sample. Reduced chi-square values near 1 signify a good fit quality. This figure also shows the values for AGN properties, such as bolometric luminosity (L_{Bol}) and accretion luminosity (L_{Acc}), from which we calculated the Eddington ratio (λ_{EDD}) for each source.

Galaxies with fits resulting in $\chi^2_{\text{red}} > 5$ were excluded from the analysis, leading to the exclusion of only three galaxies out of the initial 52: NGC4013, NGC4826, and NGC5866. NGC4013 and NGC5866 present challenges due to their dusty nature and pronounced side-view orientation, complicating AGN detection and subsequent SED fitting. Specifically, NGC4013 experiences additional complexity due to star contamination near its center.

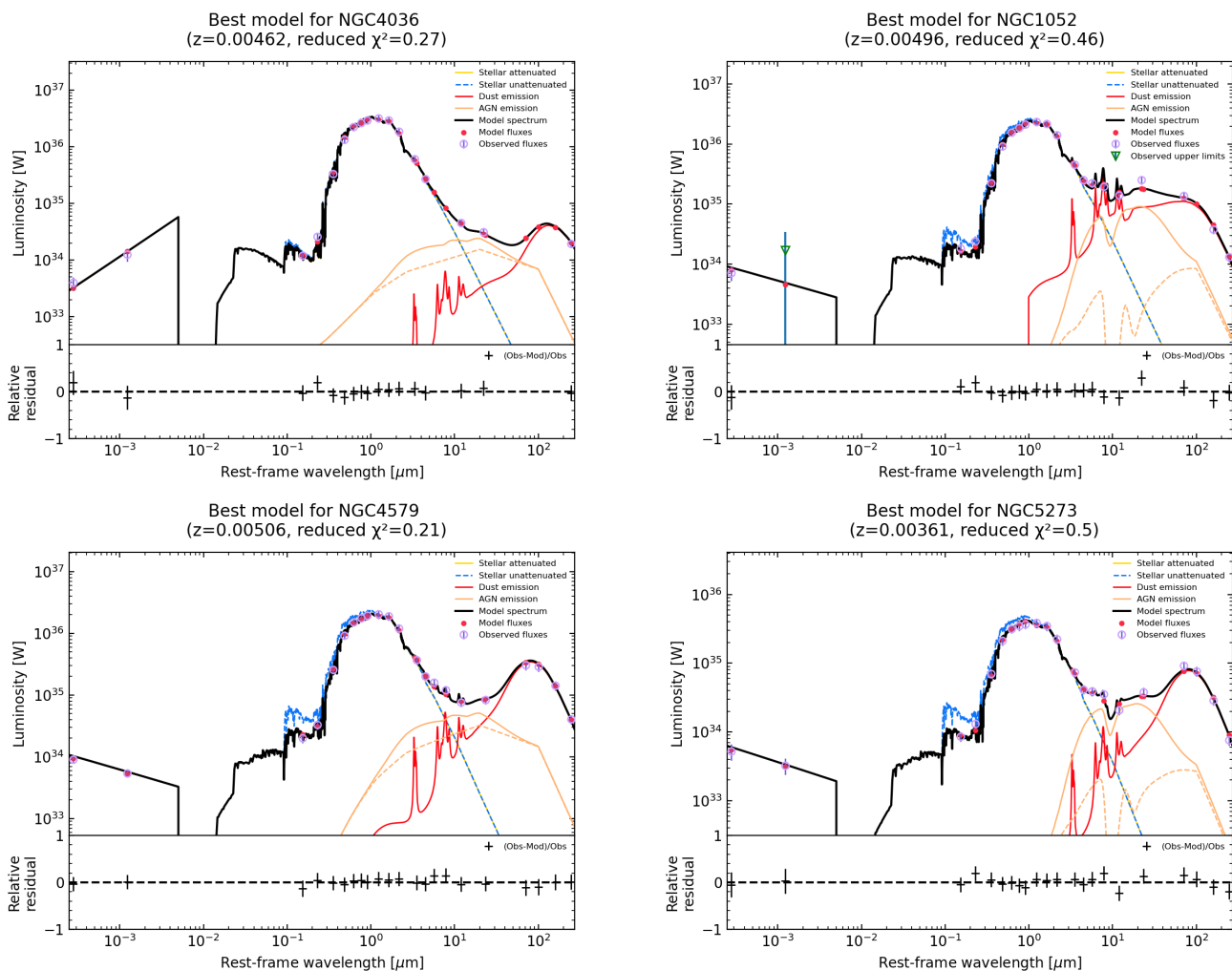


Fig. 6. Example of the best fit achieved with our module for the LLAGN sample: NGC4036 and NGC4579 are presented on the left, showcasing a direct view of the central engine ($i = 10^\circ$), with NGC4579 additionally exhibiting some dust extinction in the polar direction ($E(B - V)_{\text{polar}} = 0.3$). Conversely, on the right, NGC1052 and NGC5273 are depicted, illustrating an obscured view of the central engine ($i = 80^\circ$), highlighting the impact of viewing angle on the observed SED characteristics.

Although NGC4826 has no side-view orientation, it is characterized by a prominent absorbing dust lane.

The analysis of SED fitting results revealed a median reduced χ^2 value of 1.02 and a mean value of 1.24, affirming consistently satisfactory fit quality. Figure 5 displays the distribution of essential AGN properties, including luminosities and Eddington ratios. The accretion luminosity (L_{Acc}), representing the total radiation output of the central engine averaged across all directions, is contrasted with the bolometric luminosity (L_{Bol}), which encompasses all AGN emissions, including dust re-emission. The measured luminosities for all sources span a broad range from 10^{38} to 10^{43} erg s^{-1} . Utilizing L_{Acc} alongside M_{BH} data sourced from the literature enabled the derivation of Eddington ratios predominantly within the range of 10^{-8} to 0.001, aligning with expectations for this sample. Figure 6 offers visual confirmations of the SED fitting outcomes for a selection of galaxies, showcasing the model's proficiency in mirroring observed SED patterns. Additionally, a compilation of the primary physical parameters estimated from the CIGALE output is cataloged in Table 3.

4. Results and Discussion

This section delineates the outcomes derived from applying our novel CIGALE module, which is tailored to fit the SEDs of LLAGN. Specifically, Section 4.1 validates our methodological approach, outlines the selection of our principal hypothesis, and contextualizes our findings within the existing literature. In Section 4.2, we explore the X-ray bolometric corrections within the low-luminosity regime. Section 4.3 studies the modeled α_{OX} indices extracted from our SED fits, investigating their alignment with established scaling relations observed in QSOs. Furthermore, Section 4.4 evaluates the specific star formation rates ($s\text{SFR}$) derived from our analysis, facilitating a comparison with a sample of high-luminosity QSOs.

4.1. Validation

The incorporation of the L_X - L_{IR} relation is substantiated by the findings presented in Section 2.1. This relation establishes a robust connection between the AGN's X-ray and mid-infrared emissions, spanning at least five orders of magnitude in luminosity. It applies to a broad range of AGN types and is minimally affected by obscuration. Diverse AGN samples covering differ-

ent luminosity ranges were employed to validate its inclusion in our module.

For the high-luminosity regime ($L_{\text{Bol}} > 10^{42} \text{ erg s}^{-1}$), bolometric luminosities used for reference were derived for the SDSS and COSMOS samples using the conventional CIGALE approach (α_{ox}). In the low-luminosity regime, bolometric luminosities from Eracleous et al. (2010) were adopted for the 14 sources in common, and a bolometric correction of $k_X = 15.8$ (Ho 2009) was assumed for the remaining sources.

Figure 7 compares these bolometric luminosities with those obtained in this work. The AGN samples exhibit linear fits closely following the 1:1 relationship within the error margins. However, for the SDSS QSOs, a deviation from the 1:1 relationship is observed beyond a luminosity of $10^{45} \text{ erg s}^{-1}$. This deviation could be attributed to the increasing influence of photons from the big blue bump at higher luminosities. For the LLAGN sample, a similar luminosity trend is observed, but the reference values fall above the 1:1 relationship. Our luminosities plotted originate from AGN modeling, while the reference values are derived from observations with an angular resolution of 1 arcsec (Eracleous et al. 2010). This large aperture could introduce significant host galaxy contamination, explaining the observed offset. Additionally, the other reference values were determined using a bolometric correction larger than the one obtained in our study, a point we will discuss further in the next section.

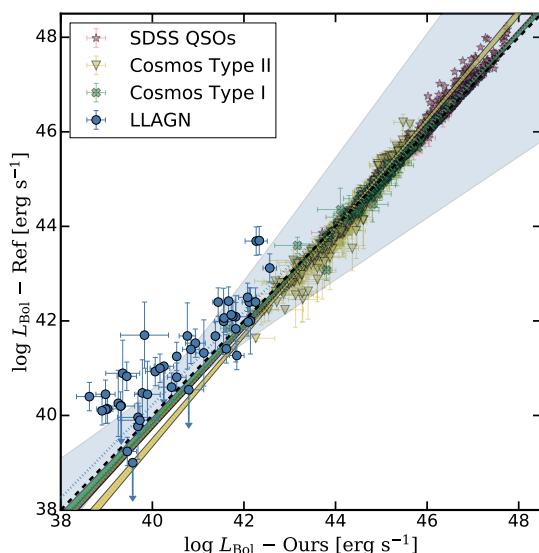


Fig. 7. Comparison of bolometric luminosities between this work and reference values. The dashed black line represents the 1:1 relation. A linear fit is shown for each sample with a dotted line following the same colors and with a shadow area of the 3-sigma deviation.

In Fig. 8, we compare the mean SEDs for the high-luminosity Type I and Type II AGN from the COSMOS sample with our LLAGN model. All SEDs include the central engine plus the toroid and polar dust emission. For the AGN sample, the conventional CIGALE approach is used; instead, the LLAGN model incorporates the ADAF+Tdk as the central engine.

The SEDs reveal distinguishing characteristics between Type I and Type II AGN. Type II AGN exhibits weaker UV-optical emission due to the torus constraining the central engine. Beyond 1 micron and into the infrared bands, both SEDs become more similar, with a subtle divergence observed in the 9.7-micron silicate complex. This feature manifests as either absorption or emission depending on the optical depth at 9.7 microns,

accompanied by a small bump emission at 50 microns for Type II AGN.

While QSOs encompass higher luminosities, both LLAGN models display comparatively lower luminosities. Initially, the mean SED of LLAGN shows characteristics of obscuration, as expected, since most LLAGN are Type II. This obscuration does not precisely match the shape of a Type II from COSMOS, exhibiting a less abrupt thermal emission at 1 micron. Transparent lines in Fig. 8 represent individual sources, revealing that some sources exhibit UV-optical slopes closer to Type II, indicative of unabsorbed ADAF. These non-obscured LLAGN showcase the expected UV shape (Fig. 2). Introducing the ADAF model brings about a notable change in the infrared, where remission from polar dust and the toroid alters the power slope of the overall AGN emission.

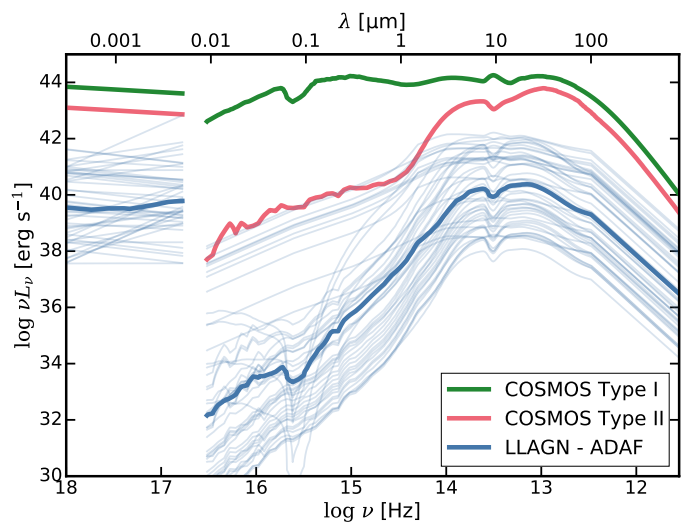


Fig. 8. Comparison of the mean SEDs fitted for QSOs from COSMOS between Type I and Type II, alongside our mean LLAGN SED using the ADAF+Tdk model. Transparent lines represent the individual SEDs of LLAGN that were fitted. X-ray emission is intrinsic and does not account for absorption.

4.2. Bolometric correction on the lower-luminosity regime

The X-ray bolometric correction (k_X) is essential for converting observed X-ray luminosity (L_X) of an AGN into its total bolometric luminosity. This correction addresses the fact that X-rays represent only a portion of the total radiation emitted by the AGN. However, X-rays play a significant role in conducting AGN surveys as AGN emissions dominate this energy band and can be easily identified. This becomes particularly vital in our LLAGN sample, where emissions from the host galaxy overshadow the UV-optical ranges, necessitating the consideration of the host galaxy's impact on bolometric luminosity.

SED fitting has proven to be an invaluable method for determining L_{Bol} of AGN. This technique comprehensively estimates total AGN luminosity as detailed in Section 3.3. By comparing L_{Bol} with L_X , we derive the bolometric correction factor k_X , such that $L_{\text{Bol}} = k_X \times L_X$. The concept of X-ray bolometric correction has been the subject of detailed investigation in studies by Hopkins et al. (2007), Lusso et al. (2012), and Duras et al. (2020). Notably, Duras et al. (2020) developed a function for k_X that leverages SED fitting incorporating an infrared-X relation within a similar framework to ours, parametrizing how k_X varies with luminosity:

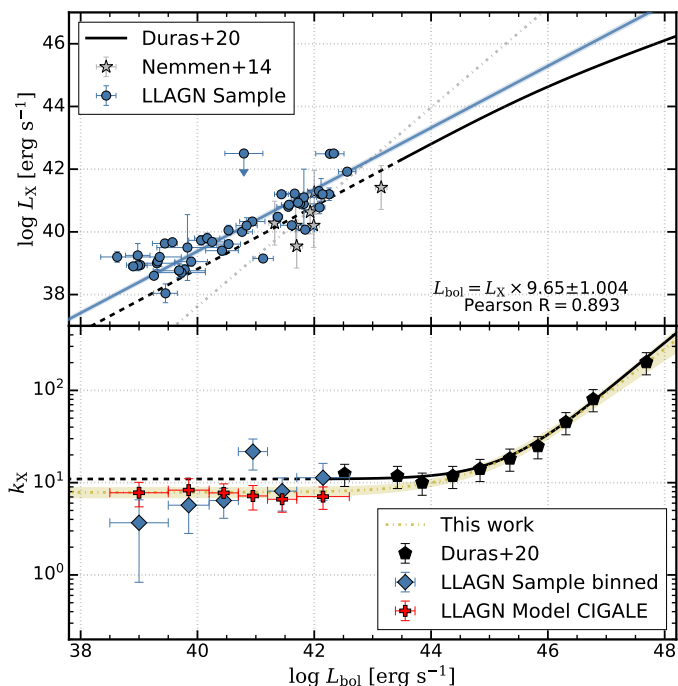


Fig. 9. Upper panel: Blue dots depict the measured X-ray luminosities plotted against the bolometric luminosities for our LLAGN sample, with a blue line indicating the linear regression fitted to this data. In contrast, the data and bolometric correction from Nemmen et al. (2014) are shown as grey stars and a dotted line, respectively. The solid black line represents the bolometric correction from Duras et al. (2020), transitioning to a dotted line where it extrapolates beyond the data. Lower panel: X-ray bolometric correction (k_X) plotted against bolometric luminosity. The solid black line denotes the bolometric correction from Duras et al. (2020), accompanied by black pentagons representing its binned data. Our binned data for the LLAGN sample are illustrated with blue diamonds. The dotted yellow line represents the fit to Eq. (5) using a combination of our binned data and that from Duras et al. (2020). Red crosses mark the binned data from the pure AGN X-ray luminosities modeled by CIGALE. Shaded regions indicate the 1-sigma uncertainties.

$$k_X(L_{\text{Bol}}) = a \left[1 + \left(\frac{\log(L_{\text{Bol}}/[\text{erg s}^{-1}])}{b} \right)^c \right]. \quad (5)$$

This formula demonstrates the dependence of k_X on bolometric luminosity, which becomes flatter below a specific luminosity threshold. Extrapolations from Duras et al. (2020) suggest a $k_X = 10.96$ for the lower luminosity regime, while Eracleous et al. (2010) and Ho (2009) propose $k_X = 50$ and $k_X = 15$, respectively.

In Fig. 9, we compare the relationship between L_{Bol} and L_X for our LLAGN sample with the sample from Nemmen et al. (2014) and the low-luminosity extrapolation from Duras et al. (2020). The Pearson correlation coefficient is approximately 0.9. A linear regression performed on our data yields:

$$L_{\text{Bol}} = (9.65 \pm 1.004) \times L_X. \quad (6)$$

This fit indicates a k_X value lower than those typically reported in the literature, yet it aligns closely, within error margins, with the extrapolation by Duras et al. (2020). Differences from previous studies can be attributed to several factors in our

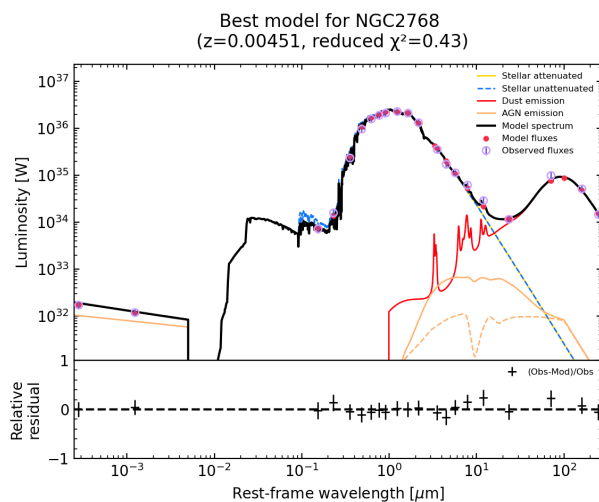


Fig. 10. Example of SED fitting for the LLAGN sample, where the host galaxy can emit in the X-ray hard band, modifying the contribution of an AGN to this band.

methodology: our specific modeling of the accretion process, a larger sample size that reduces the impact of statistical fluctuations, and the inclusion of host galaxy X-ray emissions in our modeling.

Our fit of k_X , as illustrated in the lower panel of Fig. 9, combines our observational binned data from the lower-luminosity regime with the high-luminosity binned data from Duras et al. (2020). This comprehensive approach allows us to provide an expression for k_X that spans nearly ten orders of magnitude in luminosity. The fitting achieves a χ^2 of 0.73, with parameters $a = 7.85 \pm 0.95$, $b = 45.04 \pm 0.27$, and $c = 55.87 \pm 6.64$. The binned data, comprising observational L_X and L_{Bol} derived from SED fitting, reveal a lower k_X value in the first bin, indicative of the host galaxy’s X-ray emission becoming comparable to that of the AGN and influencing the relationship. This underscores the significant role of host galaxy X-ray contributions, primarily from X-ray binaries, in shaping the bolometric correction calculation.

We also plot the k_X values obtained from modeling pure AGN X-ray emissions in CIGALE, yielding a mean $k_X \sim 7.5$. This value closely aligns with our fit, emphasizing the consistency of our approach in modeling the AGN and host galaxy X-ray emissions and their collective impact on the bolometric correction. CIGALE considers that the host galaxy X-ray emission is primarily produced by low-mass X-ray binaries (LMXBs), high-mass X-ray binaries (HMXBs), and hot gas (Yang et al. 2020). The CIGALE X-ray module utilizes the recipe from Mezcua et al. (2018) to model X-ray emission from these components, with luminosities for LMXBs and HMXBs described as functions of stellar age and metallicity. In contrast, the hot gas emission is quantified in terms of SFR. While shocks produced, for example, by a supernova and AGN feedback, can produce X-ray emission, CIGALE does not yet include shock models. Figure 10 showcases sources where the hard X-ray band significantly contributes to the host galaxy’s X-ray emission, demonstrating CIGALE’s capability to distinguish between LLAGN and host galaxy contributions, thereby refining the bolometric correction calculation.

The debate surrounding the accretion mechanisms in LLAGN motivated the inclusion of an ADAF and the possibility of a truncated thin disk, as elaborated in Section 2.2. Al-

though it is hypothesized that all sources in our sample undergo a non-standard form of accretion, only 60% have independent evidence supporting this premise. To assess the potential for a traditional accretion mechanism, we implemented a SED fitting approach that utilizes the L_X – $L_{12\mu\text{m}}$ correlation and a standard accretion disk. This approach incorporates the Schartmann et al. (2005) accretion disk model with adjustments in the optical slope ($\delta_{\text{AGN}} = -0.36, 0.36$). Analysis of the reduced chi-square values revealed comparable fitting quality between the ADAF and conventional disk accretion models, highlighting a limitation in employing SED fitting as a discriminant between these models. Moreover, the bolometric luminosities derived from both ADAF and disk models are within error margins of each other. It is noteworthy, however, that bolometric luminosities obtained via the disk model are marginally higher, exhibiting an average difference of 0.1 dex. This finding indicates a notable consistency in bolometric corrections across different accretion scenarios.

This comparison reveals that although the distribution of UV-to-IR photons may vary, the total integrated luminosity exhibits no significant dependency on the chosen accretion model. This independence arises because the L_X – $L_{12\mu\text{m}}$ relationship, which serves as a foundational prior for AGN emission, effectively balances the SED profile. This equilibrium compensates for the lack of UV photons with an increased presence of IR emissions, resulting in a bolometric correction that remains unaffected by the accretion mode. This finding underscores the model-independence of bolometric corrections, emphasizing their reliability across different accretion regimes.

4.3. Galaxy contamination

Exploring the influence of different photometric apertures on the SED fitting for our LLAGN sample sheds light on how solid this module is for future applications. We specifically evaluated how different the AGN properties obtained from our 9-arcsec central photometry are from those obtained from entire galaxy photometry provided by DustPedia.

Figure 11 compares bolometric luminosities calculated using these two distinct methods. The congruence observed between the results signifies that our module effectively discerns the LLAGN bolometric luminosities across a wide luminosity range. Moreover, the findings from the aperture-based method closely mirror those acquired through full galaxy photometry. However, the full galaxy photometry seems to have lower luminosities than the central aperture but follows the 1:1 relation within the uncertainties, suggesting minimal discrepancy within the bounds of error.

This consistency in bolometric luminosity estimation becomes particularly pertinent for sources at higher redshifts. At such distances, an instrument’s PSF might encapsulate emissions from the central regions and the periphery of galaxies, potentially complicating the task of distinctly resolving galactic structures. Despite these challenges, the IRX module demonstrates a steadfast capability to accurately estimate bolometric luminosities, demonstrating its effectiveness even when full galaxy photometry is employed. These observations highlight the utility of this module when the photometry accounts for the galaxy’s total emitted flux, extending its applicability to high-redshift observations.

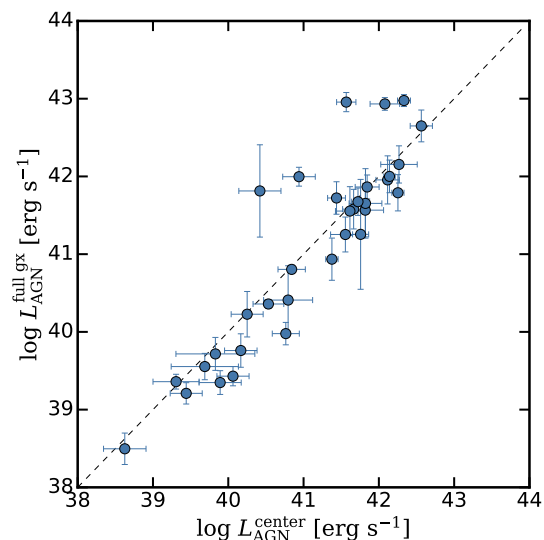


Fig. 11. Comparison of bolometric luminosities obtained using a central aperture-based photometric approach and entire galaxy photometry for the LLAGN sample. The dotted line represents the 1:1 relationship. Excluding a few outliers, our sources generally exhibit lower luminosities for the entire galaxy fit but align with the 1:1 relation within uncertainties. This suggests that bolometric luminosity can be accurately estimated even in scenarios with significant host galaxy contamination.

4.4. α_{OX} in Low-Luminosity AGN

Our approach does not dictate a specific value for α_{OX} but instead facilitates the reconstruction of the modeled 2500-Å emission at its core to compare with the 2 keV emission. This methodology allows for examining the α_{OX} behavior within the modeled framework, offering predictions for the low-luminosity domain.

The fundamental premise of the α_{OX} – L_{UV} relationship is the interplay between 2 keV and 2500 Å emissions. Figure 12 delineates this association and juxtaposes it with the linear correlations observed in both high and low-luminosity regimes, as reported by studies such as Lusso et al. (2010), Just et al. (2007), and Xu (2011). Our analysis reveals a shift towards lower UV luminosities for comparable X-ray luminosity levels. The equation for the linear fit to our data is as follows:

$$\log L_{\nu}(2 \text{ keV}) = (0.78 \pm 0.10) \times \log L_{\nu}(2500 \text{ \AA}) + (4.02 \pm 2.31) \quad (7)$$

Although a linear fit approximates the overall trend, the residuals indicate considerable scatter ($\sigma \sim 0.74$).

Figure 13 presents the α_{OX} relationship with UV and X-ray luminosities. In the QSO regime, a pronounced correlation exists between α_{OX} and UV luminosity, which is less apparent with X-ray luminosity. Lusso et al. (2010) found α_{OX} to loosely correlate with $L_{2500\text{\AA}}$, exhibiting more scatter with $L_{2\text{keV}}$. Xu (2011) noted a similar pattern for $L_{2500\text{\AA}}$ within the LLAGN regime, albeit with greater dispersion, while no distinct correlation emerged for $L_{2\text{keV}}$. In the QSO regime, the predominance of UV photons, primarily from the big blue bump, over corona-generated X-rays domain the relation and determines the α_{OX} .

Our findings in the lower luminosity range, as illustrated in blue in Fig. 13, uncover a weak correlation of α_{OX} with UV luminosity, characterized by a slope of 0.08 ± 0.04 , and a slight inverse correlation with X-ray luminosity, indicated by a slope -0.09 ± 0.03 . The dispersion of residuals in both cases

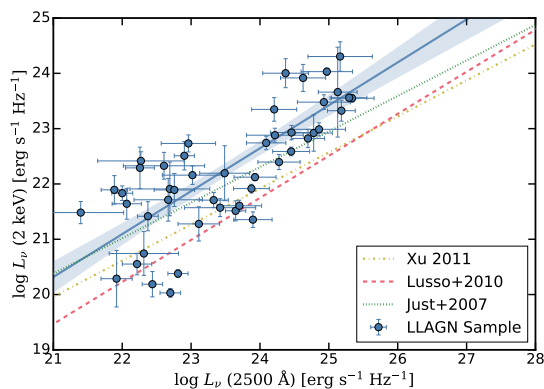


Fig. 12. Comparison of the relationship between 2 keV and 2500 Ångström emissions with Lusso et al. (2010), Xu (2011), and Just et al. (2007) data. Our linear fit is a solid blue line, with shaded regions being the uncertainties at $1\text{-}\sigma$.

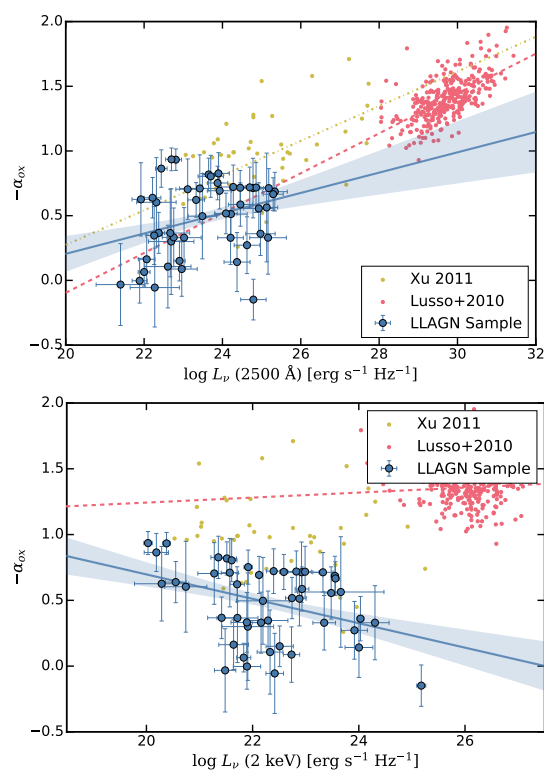


Fig. 13. Comparison of spectral index α_{ox} with 2500 Ångström luminosity (top) and two keV X-ray luminosity (bottom). The AGN sample by Lusso et al. (2010) is in red, the LLAGN sample by Xu (2011) is in yellow, and our values from the model LLAGN for each source are in blue.

is $\sigma \sim 0.27$. The α_{ox} values in LLAGN primarily range between 0 and 1, covering four X-ray and UV luminosities magnitudes. Furthermore, our data straddle the extrapolated fit from Lusso et al. (2010) in the 2500 Å luminosity plane, suggesting that neither consistent nor variable behaviors can be conclusively dismissed, especially considering the margin of error.

While UV and X-rays exhibit correlation in the high-luminosity regime, the source of X-ray photons in low-luminosity AGN may not solely be a hot corona. ADAFs are known for their pronounced emission in hard X-rays. Hence, X-ray photons in this context could stem from various processes, including inverse-Compton scattering, but operating at disparate

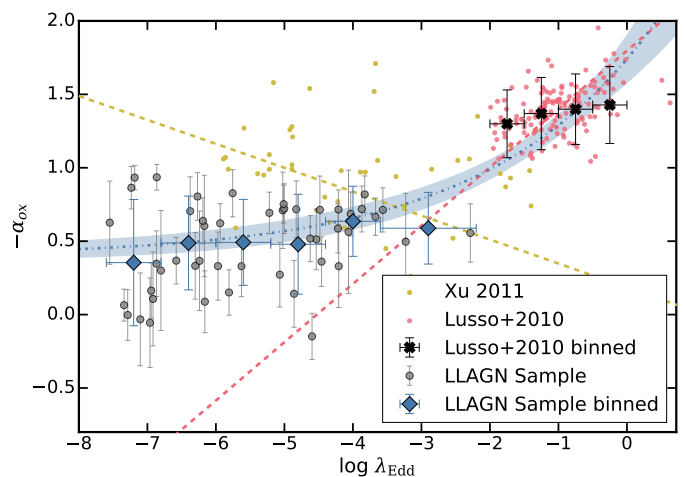


Fig. 14. Comparison of the spectral index α_{ox} with the Eddington ratio (λ_{Edd}). The AGN sample from Lusso et al. (2010) is represented in red, the LLAGN sample from Xu (2011) is in yellow, and our modeled values for each LLAGN source are in grey. Our binned data are depicted as blue diamonds, while the black crosses represent the binned data from Lusso et al. (2010). The dashed blue line indicates the fit to all the binned data. Contrary to the anticorrelation proposed by Xu (2011), our fit follows a constant value for the low regime. Shaded regions indicate the $1\text{-}\sigma$ uncertainties.

scales. This complexity could account for the observed significant dispersion in the $L_{2\text{keV}}\text{-}L_{2500\text{\AA}}$ relationship.

We further examine the $\alpha_{\text{ox}}\text{-}\lambda_{\text{Edd}}$ domain to gain deeper insights. The correlation found in QSOs sources by Lusso et al. (2010), where sources with higher accretion rates showcase elevated α_{ox} values, corroborates the notion that increased accretion intensifies the big blue bump, thereby boosting UV photon production. In contrast, an anticorrelation in LLAGN was observed by Xu (2011), suggesting a divergent behavior in this regime.

Our findings, depicted in Fig. 14, reveal that LLAGN tend to exhibit either a mild correlation or maintain constant α_{ox} values across different accretion rates. By binning our data, combining it with the data retrieved by Lusso et al. (2010), and applying a broken power-law fit, we capture behavior spanning nine orders of magnitude in λ_{Edd} . The equation fitted is:

$$-\alpha_{\text{ox}}(\lambda_{\text{Edd}}) = a \left[1 + \left(\frac{\log(\lambda_{\text{Edd}})}{b} \right)^c \right]. \quad (8)$$

Since the accretion regime is supposed to switch at $\log \lambda_{\text{Edd}} = -3$, we anchor $b = 0.001$. The fit yields a χ^2 of 0.4, characterized by parameters $a = 0.39 \pm 0.03$ and $c = 0.18 \pm 0.03$. Figure 14 showcases the behavior of the relation.

This outcome is consistent with the UV/X-ray correlation depicted in Fig. 12, suggesting a stable ratio between these emissions and a uniform α_{ox} . Whereas in conventional QSOs, variations in accretion rates can modify the big blue bump across the UV-optical spectrum, in the low-luminosity regime, the accretion flows predominantly generate the optical/UV photons. This process involves the inverse Compton scattering of soft synchrotron photons by hot electrons within the ADAF, a phenomenon governed more by magnetic field dynamics than by mass influx into the flow.

Nonetheless, a deeper exploration is warranted to grasp the ramifications of this accretion paradigm fully. Measuring UV emissions in LLAGN is complicated by their inherently faint nature, and our analysis leverages ADAF-centric modeling. For

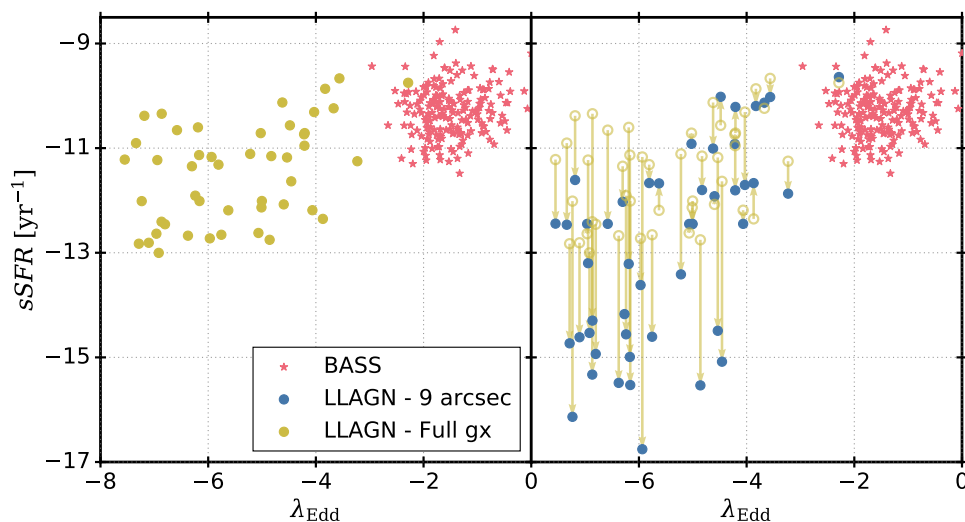


Fig. 15. Comparison of specific star formation rate ($sSFR$) versus Eddington ratios across different luminosities and photometry methods. In the left panel, high-luminosity AGN from the BASS survey is represented by red stars, while the LLAGN sample, derived from full-galaxy photometry, is shown as yellow dots. The right panel illustrates the adjustment of $sSFR$ for the LLAGN sample when central photometry is applied. Yellow arrows indicate the shift from the initial $sSFR$ values (yellow empty dots) to the recalculated values (blue dots), highlighting a possible localized impact of LLAGN on star formation rates within the galaxy’s central regions.

instance, the study by Xu (2011) relies on UV luminosity estimations derived from optical photon proxies, like continuum or emission lines. Future research employing high-resolution data across UV, optical, and infrared spectrums from instruments like the *Hubble Space Telescope* (HST) and the *James Webb Space Telescope* (JWST), will be crucial for more accurately delineating the SED in the central parsec of these galaxies.

4.5. LLAGN effects in SFR

AGN feedback is known to affect the SFR of host galaxies, with even LLAGN capable of influencing their environments. Instances such as NGC4579 (Ogle et al. 2024) demonstrate how radio jets can impact the ISM, suppressing star formation within the galaxy’s inner disk. Similarly, Almeida et al. (2023) have shown that the diminished radiative power characteristic of an ADAF can effectively hinder star formation by heating and ionizing surrounding gas. However, the precise dynamics between LLAGN activity and SFR remain partially understood.

Figure 15 showcases a comparative analysis of the specific star formation rate ($sSFR = SFR/M_*$) versus the Eddington ratio for the selected sample of LLAGN. The $sSFR$ is derived for different apertures from the complete galaxy aperture data sourced from Dustpedia (first panel) and those derived from our targeted central nine arcsec photometry (second panel). Given our sample’s average distance, the latter encompasses an effective area roughly equivalent to a 1.5 kpc diameter.

To contextualize our findings within the broader AGN spectrum, we compare these results against a sample of high-luminosity AGN from the BASS survey (Koss et al. 2022a,b). This comparison is pertinent, as our sample and the BASS survey’s local X-ray detected AGN at similar evolutionary stages within their respective host galaxies. Utilizing high-luminosity AGN data from the BASS survey along with their corresponding host galaxy properties (Koss et al. 2021), it appears that a relation exists across different Eddington ratios, wherein the $sSFR$ calculated for the entire galaxy increases by at least two orders of magnitude at higher Eddington ratios. This trend suggests the

existence of underlying feedback or fueling dynamics that interlink star formation with SMBH accretion processes.

Nevertheless, for most of the LLAGN in our sample, the $sSFR$ experiences a significant drop (approximately -1.4 dex from its mean value) when calculated from 9 arcsec photometry. This is illustrated in the second panel of Figure 15, where arrows indicate the change in integrated $sSFR$ versus the central $sSFR$ for each source, predominantly showing a decrease along the $sSFR$ axis. This pattern suggests that LLAGN may predominantly suppress star formation in the central regions of their host galaxies.

These findings indicate that the influence of AGN on star formation extends beyond high-luminosity sources, with LLAGN also affecting their host galaxies’ SFRs—primarily within central regions. This impact might also stem from prior AGN activity, leaving an altered LLAGN and ISM as a remnant of such events. Future investigations leveraging the $H\alpha$ emission as a proxy for the historical activity of the fading AGN (Esparza-Arredondo et al. 2020) could offer further insights into the specifics of each scenario. Nonetheless, a rigorous comparison with inactive galaxies is necessary to address this trend comprehensively. This study only aims to introduce a novel approach to SED modeling for LLAGN and explore its potential applications, leaving a detailed examination of the mechanisms affecting and suppressing star formation for subsequent research.

5. Summary and Conclusions

This work introduces an innovative CIGALE code module tailored to analyze low-luminosity AGN. By implementing empirical relationships and physically-based accretion models, this module enhances our understanding of LLAGN through SED fitting, avoiding commonly used QSO extrapolation. Key findings from our comparison of local LLAGN properties to those of QSOs using this new module include the following:

1. The creation of a specialized CIGALE module for LLAGN SED fitting. This development leverages the empirical $L_X-L_{12\mu m}$ relationship to link AGN X-ray and infrared emissions.

It introduces the option of modeling the central engine with both an ADAF and a truncated accretion disk.

2. A comprehensive dataset of 52 X-ray-detected local galaxies, primarily LINERs and Seyferts, was compiled to test and affirm the module's accuracy in lower luminosity ranges. Comparison of these with higher luminosity AGN from the COSMOS and SDSS samples facilitated a robust comparative analysis, validating the module's effectiveness through its alignment with established reference values.
3. The new module demonstrated exceptional precision in estimating LLAGN bolometric luminosities, effectively mitigating galaxy contamination. This is particularly noteworthy in cases where the central aperture might not entirely capture galaxy emissions (refer to Section 4.3).
4. We expand the X-ray to bolometric correction formula to the lower luminosity regime, arriving to do it applicable across ten orders of L_{Bol} . While this formula shows lower values of k_X for LLAGN than other assumed values, it is consistent with extrapolations for high-luminosity AGN from similar methodology studies. Our method is compared with standard accretion models, underscoring the robustness and model independence in characterizing the AGN emission across all ranges of luminosities (refer to Fig. 9).
5. The analysis of the α_{ox} index revealed patterns that deviate from those seen in the high-luminosity regime. Unlike in QSOs, where α_{ox} demonstrates a correlation with λ_{Edd} , in LLAGN, α_{ox} tends to remain constant or exhibit only weak correlations. This difference may indicate a shift in accretion physics and photon production mechanisms within LLAGN environments (see Fig. 14).
6. The $sSFR$ decreases by 1.4 dex in mean value from an aperture that includes the entire galaxy to one with a diameter of approximately 1.5 kpc. This suggests a potential feedback mechanism from present or past AGN activity localized at the center of these galaxies (refer to Fig. 15).

Our findings substantially advance the characterization and comprehension of LLAGN, a category of active galactic nuclei with significant analytical challenges. These insights pave the way for future explorations into LLAGN's distinctive attributes and impacts, emphasizing the critical role of a multi-wavelength perspective in AGN research.

Acknowledgements. We kindly thank Dra. Cristina Ramos-Almeida, for valuable comments and discussion on this work. This action has received funding from the European Union's Horizon 2020 research and innovation programme under Marie Skłodowska-Curie grant agreement No 860744 "Big Data Applications for Black Hole Evolution Studies" (BiD4BEST⁶) and the European Union's Horizon 2020 research and innovation program under grant agreement no. 101004168, the XMM2ATHENA project. The color schemes used in this work are color-blind friendly from Paul Tol's Notes⁷. We also acknowledge the use of computational resources from the parallel computing cluster of the Open Physics Hub⁸ at the Physics and Astronomy Department of the University of Bologna. EB acknowledges the support of the INAF Large Grant 2022 "The metal circle: a new sharp view of the baryon cycle up to Cosmic Dawn with the latest generation IFU facilities". SB acknowledges support from the Spanish Ministerio de Ciencia e Innovación through project PID2021-124243NB-C21.

References

Agüero, E. L., Díaz, R. J., & Bajaja, E. 2004, *A&A*, 414, 453
 Aird, J., Coil, A. L., Moustakas, J., et al. 2012, *ApJ*, 746, 90
 Alexander, D. M. & Hickox, R. C. 2012, *New A Rev.*, 56, 93

⁶ <https://www.bid4best.org/>

⁷ <https://personal.sron.nl/~pault/>

⁸ <https://site.unibo.it/openphysicshub/en>

- Alexander, T., Sturm, E., Lutz, D., et al. 1999, *ApJ*, 512, 204
 Almeida, I., Nemmen, R., & Riffel, R. A. 2023, *MNRAS*, 526, 217
 Annuar, A., Alexander, D. M., Gandhi, P., et al. 2020, *MNRAS*, 497, 229
 Asmus, D., Gandhi, P., Hönic, S. F., Smette, A., & Duschl, W. J. 2015, *MNRAS*, 454, 766
 Baldi, R. D., Williams, D. R. A., Beswick, R. J., et al. 2021a, *MNRAS*, 508, 2019
 Baldi, R. D., Williams, D. R. A., McHardy, I. M., et al. 2018, *MNRAS*, 476, 3478
 Baldi, R. D., Williams, D. R. A., McHardy, I. M., et al. 2021b, *MNRAS*, 500, 4749
 Boquien, M., Burgarella, D., Roehly, Y., et al. 2019, *A&A*, 622, A103
 Bu, D.-F. & Yang, X.-H. 2019, *ApJ*, 871, 138
 Cao, X. & Wang, J.-X. 2014, *MNRAS*, 444, L20
 Cappi, M., Panessa, F., Bassani, L., et al. 2006, *A&A*, 446, 459
 Chabrier, G. 2003, *PASP*, 115, 763
 Chang, H.-Y., Choi, C.-S., & Yi, I. 2002, *AJ*, 124, 1948
 Doi, A., Kameno, S., Kohno, K., Nakanishi, K., & Inoue, M. 2005, *MNRAS*, 363, 692
 Duras, F., Bongiorno, A., Ricci, F., et al. 2020, *A&A*, 636, A73
 Eracleous, M., Hwang, J. A., & Flohic, H. M. L. G. 2010, *ApJS*, 187, 135
 Esparza-Arredondo, D., Osorio-Clavijo, N., González-Martín, O., et al. 2020, *ApJ*, 905, 29
 Fabian, A. C. 2012, *ARA&A*, 50, 455
 Falocco, S., Larsson, J., & Nandi, S. 2020, *A&A*, 638, A67
 Feltre, A., Hatziminaoglou, E., Fritz, J., & Franceschini, A. 2012, *MNRAS*, 426, 120
 Fernández-Ontiveros, J. A., López-López, X., & Prieto, A. 2023, *A&A*, 670, A22
 Gandhi, P., Horst, H., Smette, A., et al. 2009, *A&A*, 502, 457
 Giroletti, M. & Panessa, F. 2009, *ApJ*, 706, L260
 González-Martín, O., Masegosa, J., Márquez, I., Guainazzi, M., & Jiménez-Bailón, E. 2009, *A&A*, 506, 1107
 Goold, K., Seth, A., Molina, M., et al. 2023, arXiv e-prints, arXiv:2307.01252
 Haardt, F. & Maraschi, L. 1991, *ApJ*, 380, L51
 Haardt, F. & Maraschi, L. 1993, *ApJ*, 413, 507
 Hauschild Roier, G. R., Storchi-Bergmann, T., McDermid, R. M., et al. 2022, *MNRAS*, 512, 2556
 Heckman, T. M. & Best, P. N. 2014, *ARA&A*, 52, 589
 Hickox, R. C. & Alexander, D. M. 2018, *ARA&A*, 56, 625
 Ho, L. C. 1999, *Advances in Space Research*, 23, 813
 Ho, L. C. 2008, *ARA&A*, 46, 475
 Ho, L. C. 2009, *ApJ*, 699, 626
 Hopkins, P. F., Richards, G. T., & Hernquist, L. 2007, *ApJ*, 654, 731
 Ishibashi, W., Auger, M. W., Zhang, D., & Fabian, A. C. 2014, *MNRAS*, 443, 1339
 Jones, A. P., Köhler, M., Ysard, N., Bocchio, M., & Verstraete, L. 2017, *A&A*, 602, A46
 Just, D. W., Brandt, W. N., Shemmer, O., et al. 2007, *ApJ*, 665, 1004
 Kammoun, E. S., Miller, J. M., Koss, M., et al. 2020, *ApJ*, 901, 161
 Koss, M. J., Ricci, C., Trakhtenbrot, B., et al. 2022a, *ApJS*, 261, 2
 Koss, M. J., Strittmatter, B., Lamperti, I., et al. 2021, *ApJS*, 252, 29
 Koss, M. J., Trakhtenbrot, B., Ricci, C., et al. 2022b, *ApJS*, 261, 1
 Laigle, C., McCracken, H. J., Ilbert, O., et al. 2016, *ApJS*, 224, 24
 Liu, H. & Wu, Q. 2013, *ApJ*, 764, 17
 López, I. E., Brusa, M., Bonoli, S., et al. 2023, *A&A*, 672, A137
 Lusso, E., Comastri, A., Simmons, B. D., et al. 2012, *MNRAS*, 425, 623
 Lusso, E., Comastri, A., Vignali, C., et al. 2010, *A&A*, 512, A34
 Mahmoud, R. D. & Done, C. 2020, *MNRAS*, 491, 5126
 Maoz, D. 2007, *MNRAS*, 377, 1696
 Marchesi, S., Civano, F., Elvis, M., et al. 2016, *ApJ*, 817, 34
 Masini, A., Wijesekera, J. V., Celotti, A., & Boorman, P. G. 2022, *A&A*, 663, A87
 Mason, R. E., Lopez-Rodriguez, E., Packham, C., et al. 2012, *AJ*, 144, 11
 Masoura, V. A., Mountrichas, G., Georgantopoulos, I., & Plionis, M. 2021, *A&A*, 646, A167
 Meyer-Hofmeister, E. & Meyer, F. 2011, *A&A*, 527, A127
 Mezcuca, M., Civano, F., Marchesi, S., et al. 2018, *MNRAS*, 478, 2576
 Mountrichas, G., Buat, V., Yang, G., et al. 2022, *A&A*, 663, A130
 Mukherjee, D., Bicknell, G. V., Wagner, A. Y., Sutherland, R. S., & Silk, J. 2018, *MNRAS*, 479, 5544
 Nemmen, R. S., Storchi-Bergmann, T., & Eracleous, M. 2014, *MNRAS*, 438, 2804
 Niedźwiecki, A., Stępnik, A., & Xie, F.-G. 2015, *ApJ*, 799, 217
 Novak, G. S., Ostriker, J. P., & Ciotti, L. 2011, *ApJ*, 737, 26
 Ogle, P. M., López, I. E., Reynaldi, V., et al. 2024, *ApJ*, 962, 196
 Osorio-Clavijo, N., González-Martín, O., Sánchez, S. F., Guainazzi, M., & Cruz-González, I. 2023, *MNRAS*, 522, 5788
 Pacifici, C., Iyer, K. G., Mobasher, B., et al. 2023, *ApJ*, 944, 141
 Padovani, P., Alexander, D. M., Assef, R. J., et al. 2017, *A&A Rev.*, 25, 2

- Pâris, I., Petitjean, P., Aubourg, É., et al. 2018, *A&A*, 613, A51
- Pellegrini, S. 2005, *ApJ*, 624, 155
- Peterson, B. M. 1997, *An Introduction to Active Galactic Nuclei*
- Peterson, B. M., McHardy, I. M., Wilkes, B. J., et al. 2000, *ApJ*, 542, 161
- Ptak, A. 2001, in *American Institute of Physics Conference Series*, Vol. 599, *X-ray Astronomy: Stellar Endpoints, AGN, and the Diffuse X-ray Background*, ed. N. E. White, G. Malaguti, & G. G. C. Palumbo, 326–335
- Ramos Almeida, C. & Ricci, C. 2017, *Nature Astronomy*, 1, 679
- Reynaldi, V., Guainazzi, M., Bianchi, S., et al. 2020, *MNRAS*, 499, 5107
- Ricci, C., Trakhtenbrot, B., Koss, M. J., et al. 2017, *ApJS*, 233, 17
- Schartmann, M., Meisenheimer, K., Camenzind, M., Wolf, S., & Henning, T. 2005, *A&A*, 437, 861
- Schawinski, K., Lintott, C. J., Thomas, D., et al. 2009, *ApJ*, 690, 1672
- Stalewski, M., Fritz, J., Baes, M., Nakos, T., & Popović, L. Č. 2012, *MNRAS*, 420, 2756
- Stalewski, M., Ricci, C., Ueda, Y., et al. 2016, *MNRAS*, 458, 2288
- Szanecki, M., Niedźwiecki, A., & Wojaczyński, R. 2023, *MNRAS*, 521, 2215
- Szanecki, M., Niedźwiecki, A., & Zdziarski, A. A. 2021, *ApJ*, 909, 205
- Taam, R. E., Liu, B. F., Yuan, W., & Qiao, E. 2012, *ApJ*, 759, 65
- Tran, H. D., Lyke, J. E., & Mader, J. A. 2011, *ApJ*, 726, L21
- Williams, D. R. A., Pahari, M., Baldi, R. D., et al. 2022, *MNRAS*, 510, 4909
- Wójtowicz, A., Stawarz, Ł., Cheung, C. C., Werner, N., & Rudka, D. 2023, *ApJ*, 944, 195
- Xu, Y.-D. 2011, *ApJ*, 739, 64
- Yang, G., Boquien, M., Brandt, W. N., et al. 2022, *ApJ*, 927, 192
- Yang, G., Boquien, M., Buat, V., et al. 2020, *MNRAS*, 491, 740
- Yuan, F. & Narayan, R. 2014, *ARA&A*, 52, 529
- Yuan, F., Yu, Z., & Ho, L. C. 2009, *ApJ*, 703, 1034
- Yun, S. B., Miller, J. M., Barret, D., et al. 2022, *ApJ*, 935, 12
- Zhang, F. & Wu, X.-B. 2006, *Chinese J. Astron. Astrophys.*, 6, 165

Table 2. Parameters and values for the modules used with CIGALE for the LLAGN sample.

Parameter	Model/values
Star formation history: delayed model	
Age of the main population	3000, 5000, 7000, 10000 Myr
e-folding time	100, 500, 1000, 3000 Myr
Burst stellar mass fraction	0.0, 0.1
Simple Stellar population: Bruzual & Charlot (2003)	
Initial Mass Function	Chabrier (2003)
Metallicity	0.008 (LMC), 0.02 (Solar)
Galactic dust extinction	
Dust attenuation recipe	modified Calzetti et al. (2000)
$E(B-V)_{lines}$	0.1, 0.3, 0.5, 0.7
$E(B-V)_{factor}$	0.1, 0.44, 0.7
Power-law slope modifying the attenuation curve	-0.4, 0.0
Galactic dust emission: Themis (Jones et al. 2017)	
q_{HAC}	0.02, 0.17, 0.24
U_{min}	0.1, 0.5, 2.5, 5.0, 10.0, 50.0
α slope in $dM_{dust} \propto U^{-\alpha} dU$	2.1, 2.5, 2.9
γ	0.4
AGN module: SKIRTOR	
Torus optical depth at 9.7 microns $\tau_{9.7}$	3, 7, 11
Torus opening angle	70°
Viewing angle	10° (type 1), 80° (type 2)
Disk spectrum	ADAF + Truncated disk
Delta parameter for the truncated disk	0, 1.0
AGN fraction	0.001, 0.01, 0.05, 0.1, 0.2, 0.3
Extinction law of polar dust	SMC
$E(B - V)$ of polar dust	0.0, 0.3, 0.6
Temperature of polar dust	100 K
Emissivity of polar dust	1.6
X-ray module: this paper	
AGN photon index Γ	1.6, 1.8, 2.0, 2.5, 3.0, 3.5
α_{irx}	0, 0.15, 0.3, 0.45, 0.6
Deviation from expected LMXB and HMXB	0., 0.
Total number of models per redshift	671,846,400

e

ID	$\log L_{\text{Acc}}$ [erg/s]	λ_{Edd}	$\log L_{\text{Bol}}$ [erg/s]	$\log L_{\text{X}}^{\text{mod}}$ [erg/s]	$\log L_{2500\text{\AA}}$ [erg/s Hz]	$\log L_{2\text{ keV}}$ [erg/s Hz]	α_{OX}
NGC1052	42.16 ± 0.23	8.61E-05	42.11 ± 0.15	41.13 ± 0.09	25.12 ± 0.28	23.66 ± 0.81	-0.56 ± 0.42
NGC2273	41.82 ± 0.21	3.29E-05	41.81 ± 0.24	40.90 ± 0.14	24.77 ± 0.27	22.92 ± 0.32	-0.71 ± 0.23
NGC2685	39.35 ± 0.45	6.78E-07	39.30 ± 0.30	38.47 ± 0.16	22.31 ± 0.50	20.74 ± 0.39	-0.60 ± 0.34
NGC2655	42.02 ± 0.31	3.48E-05	42.25 ± 0.08	41.20 ± 0.04	24.97 ± 0.37	24.03 ± 0.06	-0.36 ± 0.16
NGC2768	40.14 ± 0.25	4.21E-07	40.06 ± 0.21	39.17 ± 0.13	23.11 ± 0.30	21.27 ± 0.30	-0.70 ± 0.23
NGC2787	38.43 ± 0.57	7.87E-08	38.62 ± 0.28	37.87 ± 0.20	21.39 ± 0.62	21.48 ± 0.20	0.03 ± 0.31
NGC2841	38.95 ± 0.16	2.82E-08	39.02 ± 0.23	38.13 ± 0.20	21.91 ± 0.22	20.28 ± 0.51	-0.62 ± 0.28
NGC3031	40.96 ± 0.25	6.02E-06	41.12 ± 0.17	40.40 ± 0.05	23.92 ± 0.30	22.12 ± 0.06	-0.69 ± 0.14
NGC3079	40.68 ± 0.02	1.48E-04	40.53 ± 0.02	39.52 ± 0.04	23.64 ± 0.14	21.51 ± 0.18	-0.81 ± 0.12
NGC3147	42.37 ± 0.27	9.28E-05	42.56 ± 0.14	41.82 ± 0.05	25.33 ± 0.31	23.55 ± 0.06	-0.68 ± 0.14
NGC3185	40.45 ± 0.47	9.46E-06	40.41 ± 0.27	39.61 ± 0.07	23.42 ± 0.51	21.57 ± 0.16	-0.71 ± 0.26
NGC3190	41.84 ± 0.27	2.53E-05	41.84 ± 0.15	41.18 ± 0.07	24.78 ± 0.32	25.17 ± 0.08	0.14 ± 0.15
NGC3193	39.64 ± 0.54	1.20E-07	39.68 ± 0.44	38.87 ± 0.28	22.60 ± 0.58	22.32 ± 0.24	-0.10 ± 0.31
NGC3414	41.30 ± 0.26	9.92E-06	41.37 ± 0.08	40.36 ± 0.05	24.27 ± 0.30	22.39 ± 0.13	-0.72 ± 0.16
NGC3516	42.20 ± 0.41	6.20E-05	42.26 ± 0.24	41.44 ± 0.11	25.16 ± 0.46	24.30 ± 0.26	-0.32 ± 0.28
NGC3718	41.32 ± 0.31	2.91E-05	41.66 ± 0.14	41.01 ± 0.06	24.21 ± 0.41	22.88 ± 0.12	-0.51 ± 0.20
NGC3898	39.10 ± 0.14	1.13E-07	38.98 ± 0.15	38.01 ± 0.14	22.06 ± 0.21	21.64 ± 0.27	-0.16 ± 0.18
NGC3945	39.99 ± 0.34	6.89E-07	40.16 ± 0.21	39.34 ± 0.10	22.96 ± 0.39	22.73 ± 0.15	-0.08 ± 0.21
NGC3953	39.25 ± 0.14	6.45E-07	39.45 ± 0.20	38.69 ± 0.14	22.21 ± 0.21	20.55 ± 0.19	-0.63 ± 0.15
NGC3982	42.21 ± 0.13	2.73E-04	42.09 ± 0.09	41.09 ± 0.05	25.18 ± 0.20	23.32 ± 0.19	-0.71 ± 0.15
NGC4036	41.40 ± 0.28	1.38E-05	41.61 ± 0.19	40.80 ± 0.11	24.37 ± 0.33	24.00 ± 0.26	-0.14 ± 0.22
...

Table 3. Properties obtained from the SED fitting of the LLAGN sample. Luminosities in erg s^{-1} , except for monochromatic luminosities that are in $\text{erg s}^{-1} \text{Hz}^{-1}$.